Iterative Learning Control for Video-Rate Atomic Force Microscopy

Nastaran Nikooienejad, Mohammad Maroufi, and S. O. Reza Moheimani, *Fellow, IEEE*

***Abstract*—We present a control scheme for video-rate atomic force microscopy with rosette pattern. The controller structure involves a feedback internal-model-based controller and a feedforward iterative learning controller. The iterative learning controller is designed to improve tracking performance of the feedback-controlled scanner by rejecting the repetitive disturbances arising from the system nonlinearities. We investigate the performance of two inversion techniques for constructing the learning filter. We conduct tracking experiments using a two-degree-of-freedom microelectromechanical system (MEMS) nanopositioner at frame rates ranging from 5 to 20 frames per second. The results reveal that the algorithm converges rapidly and the iterative learning controller significantly reduces both the transient and steady-state tracking errors. We acquire and report a series of high-resolution time-lapsed video-rate AFM images with the rosette pattern.**

***Index Terms*—Internal model principle, iterative learning control (ILC), microelectromechanical system (MEMS) nanopositioner, nonraster scanning, rosette pattern, video-rate atomic force microscopy (AFM).**

I. Introduction

VIDEO-RATE atomic force microscopy (AFM) has enabled direct visualization of dynamic processes at extremely high resolutions [1]–[4]. Until recently, it could take up to several minutes to capture a high-resolution image with an AFM due to limitations arising from the highly resonant nature of AFMs and the conventional method of scanning, i.e., rastering. There have been significant research efforts aimed at improving the functionality of AFM for high-speed imaging [5]–[9]. In particular, nonraster scan patterns have been proposed to circumvent the drawbacks due to rastering by generating smooth trajectories that are easier to navigate for a mechanical scanner. Although nonraster scan patterns such as Lissajous [10], [11], spiral [12]–[14], and cycloid [15], [16] have been successfully implemented, more research is needed to establish their performance in video-rate sequential imaging for applications that require capturing continuous interactions with nanostructures [17].

In sequential spiral and cycloid scans, back and forth motions of the scanner impose sharp transitions at the periphery of scan area, deteriorating the resulting AFM images [8], [16]. To address common issues with sequential scanning AFM methods, we recently proposed a novel nonraster method based on the rosette pattern [18]. This repetitive pattern can be used to acquire time-lapsed AFM images without the need for undesirable back and forth motions of the positioner.

A number of control design techniques such as model predictive control [19], linear quadratic Gaussian control [20], Kalman-filter-based control [21], and internal-model-based control [13] have been successfully applied to nonraster scanning problems. In particular, promising results have been obtained with the IMBC [10], [13], [16], [22]. This controller achieves asymptotic zero steady-state tracking error by incorporating an internal model of reference signals and disturbances. However, this method requires accurate identification of disturbances, predominantly arising from unmodeled system nonlinearities [10], [13], [16], [22]. Due to the sinusoidal nature of reference signals in nonraster scan patterns, such disturbances typically contain higher harmonics of reference frequencies. Consequently, the controller needs to be redesigned when the reference frequency is changed.

Employing a learning procedure enables us to eliminate the effect of repeating disturbances without the need for performing *a priori* identification experiments and subsequent design of a new controller. The method known as iterative learning control (ILC) [23], [24] was initially proposed for dealing with robotic systems that perform repetitive tasks. Recent research has concentrated on improving the performance of such systems and their applications to other systems that involve performing repetitive tasks [25]–[30].

More recently, ILC has found applications in lateral and vertical nanopositioning for AFM [31]–[38]. In [31] and [32], an iterative learning controller is designed for a piezo-based positioner and applied to an AFM system to decrease the tracking error arising from hysteresis and vibrations. In [33], a current-cycle-feedback ILC is integrated with an H_∞ feedback controller and applied to the z-axis positioner of AFM to achieve high-precision tracking of sample profiles. Integration of ILC

Manuscript received November 18, 2019; revised March 23, 2020 and August 20, 2020; accepted September 26, 2020. Recommended by Technical Editor G. Clayton and Senior Editor X. Tan. This work was supported in part by the University of Texas at Dallas and in part by the U.S. Department of Energy's Office of Energy Efficiency and Renewable Energy (EERE) under the Advanced Manufacturing Office Award DE-EE0008322. *(Corresponding author: S. O. Reza Moheimani.)*

Nastaran Nikooienejad and S. O. Reza Moheimani are with the Erik Jonsson School of Engineering and Computer Science, The University of Texas at Dallas, Richardson, TX 75080 USA (e-mail: nastaran.nikooienejad@utdallas.edu; reza.moheimani@utdallas.edu).

Mohammad Maroufi was with the Erik Jonsson School of Engineering and Computer Science, The University of Texas at Dallas, Richardson, TX 75080 USA. He resides in San Jose, CA 95126 USA. (e-mail: mohammad.maroufi@utdallas.edu).

Color versions of one or more of the figures in this article are available online at https://ieeexplore.ieee.org.

Digital Object Identifier 10.1109/TMECH.2020.3032565

1083-4435 © 2020 IEEE. Personal use is permitted, but republication/redistribution requires IEEE permission.
See https://www.ieee.org/publications/rights/index.html for more information.

IEEE Proof

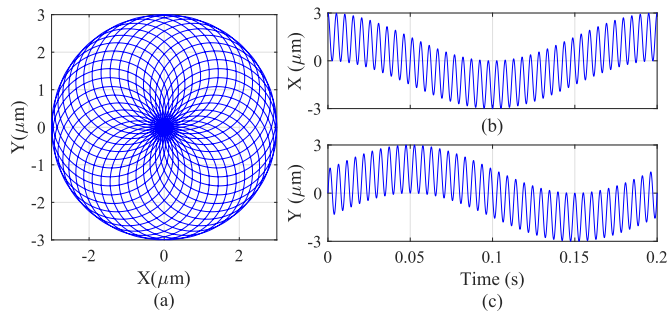

Fig. 1. (a) Rosette pattern when $R = 3\,\mu$m, $P = 250$ nm and $T = 0.2$ s. (b) and (c) Reference signals in x and y axes that generate the rosette pattern in (a).

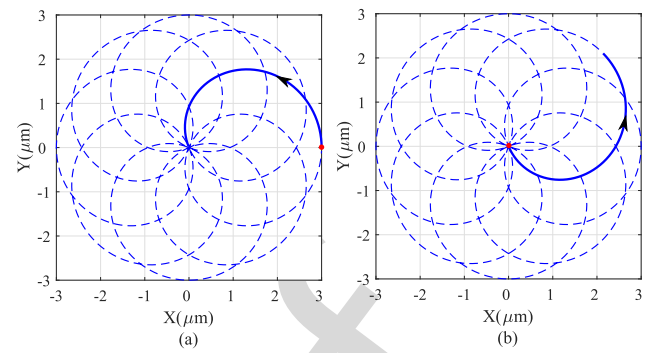

Fig. 2. (a) Rosette pattern generated from (4) starting at $(x, y) = (3, 0)$. (b) Rosette pattern generated from (7) starting at $(x, y) = (0, 0)$. The red dot (•) indicates the starting point.

with model predictive control is reported in [36] to improve the convergence rate in z-axis control of AFM. For lateral scanning, Ling *et al.* [38] propose a control scheme consisting of an integral resonant control and a PID-type ILC to augment the damping of a piezo-actuated nanopositioner. The ILC and model-based H_∞ control are combined in [39] to improve the quality of imaging in sinusoidal scanning at 80 Hz. In [37], the ILC is applied as an add-on control loop to enhance the performance of an existing PI controller for tracking an optimal spiral pattern at high frame rates.

The rest of this article is organized as follows. Section II illustrates sequential scanning with a novel nonraster scan pattern. In Section III, ILC-based control system is developed by integrating the ILC with an internal-model-based controller (IMBC) to achieve robustness against uncertainties and repetitive disturbances. In Section IV, the efficacy of the proposed approach is experimentally investigated by applying to a two-degree-of-freedom (2-DOF) microelectromechanical system (MEMS) nanopositioner. Performing high-resolution video-rate AFM imaging with a novel nonraster scan pattern is presented in Section V, and Section VI concludes this article.

To the best of the authors' knowledge, this is the first successful application of ILC to video-rate nonraster AFM imaging.

II. Sequential Scanning

To implement sequential scanning, we employ the rosette pattern [18]. In this method, the nanopositioner traverses a circular-shaped area continuously without the need for back and forth motion required in conventional raster scanning. Fig. 1 illustrates a rosette pattern and the corresponding reference signals consisting of the sum of two sinusoids with different frequencies but identical amplitudes. We can determine the amplitude and frequencies of the reference signals from the radius of the scan area (R), resolution (P), and the scan period (T). According to the design procedure described in [18], the number of petals in the rosette pattern is obtained as

$$2N = \text{Round}\left(\frac{R\pi}{P}\right). \tag{1}$$

We select N as an even integer to ensure that the pattern would cover the entire scan area. For instance, the rosette pattern in Fig. 1(a) consists of 38 overlapping petals intersecting each other at several points. For larger values of N, the number of petals increases, and high-resolution scanning is achieved.

Reference frequencies in a rosette pattern are determined from

$$\begin{aligned} f_1 &= (1+n)f \\ f_2 &= (1-n)f \end{aligned} \tag{2}$$

where f is the fundamental scan frequency, and n is selected as a rational number expressed by

$$n = \frac{N}{N+1}, \quad N \in \{2, 4, \ldots, 2\,k, \ldots\}. \tag{3}$$

Finally, the lateral axes of the nanopositioner are actuated by the following references:

$$\begin{aligned} x(t) &= \frac{R}{2}\left[\cos(2\pi f_1 t) + \cos(2\pi f_2 t)\right] \\ y(t) &= \frac{R}{2}\left[\sin(2\pi f_1 t) + \sin(2\pi f_2 t)\right]. \end{aligned} \tag{4}$$

From (2) and (4), the total scan time with the rosette pattern is obtained as

$$T = \frac{N+1}{f}. \tag{5}$$

Fig. 1(b) and (c) depicts $x(t)$ and $y(t)$ for a rosette pattern with $R = 3\,\mu$m, $P = 250$ nm, and $T = 0.2$ s.

To trace the rosette pattern, the starting point is at $(x, y) = (R, 0)$ according to (4). Then, the pattern repeats itself continuously from that point on; see Fig. 2(a). Since the nanopositioner rests at $(x, y) = (0, 0)$ when in equilibrium, we need to move it to the starting point each time it returns to the initial position. One approach is to multiply the references with a trapezoidal signal to move the positioner to the starting point linearly and decrease the reference amplitude to zero after sequential scanning is completed [40].

An alternative is to take advantage of the rosette pattern's periodicity by adding a constant phase to the reference signals in both axes to force the pattern to start at $(x, y) = (0, 0)$, as shown in Fig. 2(b). The phase shift is equivalent to the time duration required for the rosette to traverse half of a petal. As explained in [18], it takes $\frac{1}{2nf}$ (s) to draw a petal. Hence, the

IEEE Proof

phase shift corresponding to half of this duration is obtained as

$$\phi_1 = \frac{\pi(1+n)}{2n}, \quad \phi_2 = \frac{\pi(1-n)}{2n} \tag{6}$$

for the first and the second sinusoid in the reference signals. Consequently, reference signals that generate a rosette pattern starting at $(x, y) = (0, 0)$ are

$$\begin{aligned} x(t) &= \frac{R}{2}\left[\cos(2\pi f_1 t + \phi_1) + \cos(2\pi f_2 t + \phi_2)\right] \\ y(t) &= \frac{R}{2}\left[\sin(2\pi f_1 t + \phi_1) + \sin(2\pi f_2 t + \phi_2)\right]. \end{aligned} \tag{7}$$

In this article, the nanopositioner is driven to follow the reference signals in (7) to scan a circular-shaped area with a diameter of $6\,\mu$m and a scan resolution of 50 nm at frame rates ranging from 5 to 20 fps. We employ the ILC method discussed in the following section combined with a feedback controller to improve the tracking performance of the nanopositioner.

III. Control Design

Although inversion based techniques are intuitive and can be easily implemented, their efficacy depends on the accuracy of the estimated plant dynamics. Iterative techniques such as ILC improve tracking in the presence of unmodeled system nonlinearities through learning from past experiences. However, being an open-loop controller, the ILC cannot guarantee robustness against stochastic nonrepeating disturbances. This issue can be addressed by combining the ILC with a feedback controller. The feedback controller should be capable of tracking the reference signals at high speed and, given the sinusoidal nature of those signals, it should be able to achieve this objective with low bandwidth. The internal-model-based controller (IMBC) is well-suited for this purpose. By limiting closed-loop bandwidth, this controller minimizes the effect of projected sensor noise on positioning resolution.

Despite the many advantages of IMBC, this controller cannot deal with exogenous disturbances and system nonlinearities. To achieve robustness, a model of disturbances needs to be included in the feedback controller. This requires extensive experiments and typically results in a very high-order controller [13].

In this section, we design the IMBC to track the fundamental frequencies of the reference signals and achieve acceptable performance and good stability margins. Then, we proceed to design the ILC and integrate it with IMBC. We investigate the convergence properties of this control scheme to ensure satisfactory results. The proposed control scheme is suitable for both single-frame and sequential AFM imaging.

A. MEMS Nanopositioner

To experimentally investigate the controller's performance, we employ a 2-DOF MEMS nanopositioner whose design and characterization are described in detail in [5] and [41]. In this device, four electrostatic actuators move the stage bidirectionally along its lateral axes and on-chip bulk piezoresistive sensors measure the stage displacement with nanoscale precision.

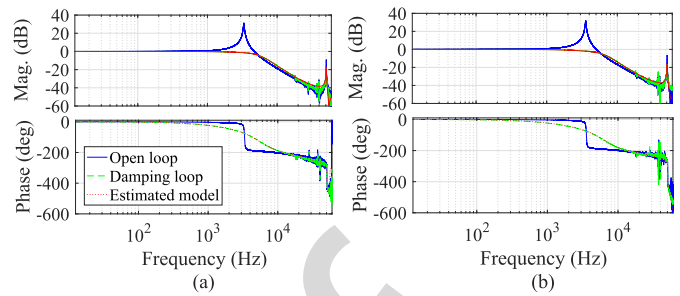

Fig. 3. Frequency response of the nanopositioner from the actuation voltage to sensor output in open loop, with the damping loop and the estimated model of the damped system in (a) x axis and (b) y axis.

Sensor calibration factors are obtained as $0.2176\,\mathrm{V}/\mu\mathrm{m}$ and $0.1958\,\mathrm{V}/\mu\mathrm{m}$ for the x and y axes, respectively.

Frequency response of the scanner is measured by applying a wide-band chirp signal and recording the sensor output using a fast Fourier transform (FFT) analyzer. Fundamental resonant frequencies of the scanner are at 3.34 kHz and 3.57 kHz for x and y axes, respectively; see Fig. 3. As described in [16], [20], and [21], we use an analog controller to add damping to this highly resonant system resulting in a closed-loop bandwidth of approximately 4.5 kHz. We then identify a dynamical model of the damped system that is a good fit up to a bandwidth of 60 kHz; see Fig. 3. In order to design the ILC, the estimated model is then discretized using a zero-order hold at a sampling frequency of 90720 Hz. This results in a nonminimum phase (NMP) model with a pair of complex zeros outside the unit circle at $0.98 \pm j3.25$ and $0.54 \pm j7.11$ for x and y axes, respectively.

B. Internal-Model-Based Controller

According to the internal model principle, steady-state tracking error asymptotically tends to zero when the controller includes an internal model of the reference signals [42]. Knowing the reference *a priori*, we can design the controller by including roots of reference generating polynomial in the controller denominator and tuning the gain and zeros to place closed-loop poles at desirable locations in order to attain acceptable tracking and stability margins. Since reference signals for rosette pattern scanning consist of pure sinusoids, the controller must contain pure imaginary poles at those reference frequencies. The control loop for one axis is shown in Fig. 4(a) where C_d and C denote the damping and internal-model-based controllers, respectively. Taking Laplace transform of reference signals in (7) and assuming a proper controller with pure imaginary poles at $\pm j\omega_1$ and $\pm j\omega_2$, we obtain

$$\begin{aligned} C_x &= \frac{a_4\, s^4 + a_3\, s^3 + a_2\, s^2 + a_1 s + a_0}{(s^2+\omega_1^2)(s^2+\omega_2^2)} \\ C_y &= \frac{b_4\, s^4 + b_3\, s^3 + b_2\, s^2 + b_1 s + b_0}{(s^2+\omega_1^2)(s^2+\omega_2^2)}. \end{aligned} \tag{8}$$

Polynomial coefficients in (8) are determined based on the desired closed-loop poles and stability margins. We tune controller zeros to set the magnitude of the closed-loop response to

IEEE Proof

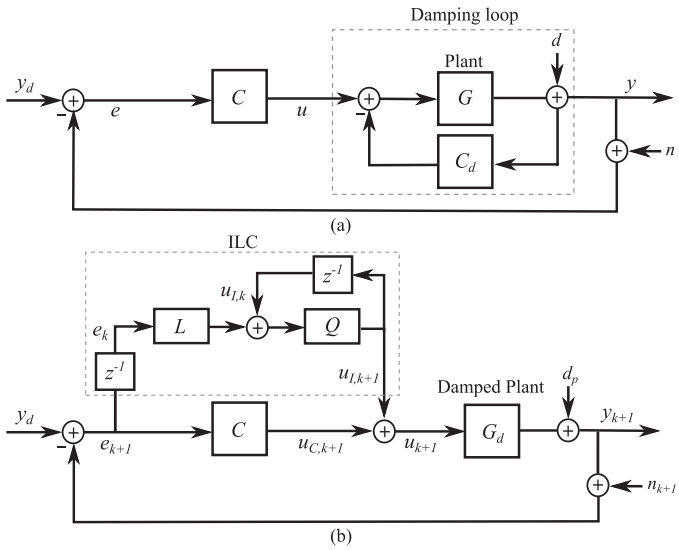

Fig. 4. (a) Control scheme with damping loop (C_d) and feedback controller (C). (b) Control scheme with the combination of iterative learning controller and feedback controller. The damped plant is modeled as G_d and the projected unmodeled disturbance is denoted by d_p. Here, L and Q are the learning and robustness filters in ILC, and z^{-1} indicates a shift in the iteration domain.

TABLE I
REFERENCE FREQUENCIES AND STABILITY MARGINS AT ALL FRAME RATES

Frame Rate	f_1 (Hz)	f_2 (Hz)		GM (dB)	PM (deg)
5 fps	945	5	C_x	17.2	100
			C_y	17.8	101
10 fps	1890	10	C_x	13.6	77.9
			C_y	14.7	80.1
15 fps	2835	15	C_x	14.5	75.8
			C_y	15.3	79.2
20 fps	3780	20	C_x	13.7	67.2
			C_y	12.9	68.9

unity at the desired reference frequencies. In Table I, we state the reference frequencies and stability margins for each frame rate. Simulated frequency responses of the x-axis closed-loop system at various frame rates are depicted in Fig. 5. The y-axis responses are similar. Although the closed-loop response at f_1 and f_2 is set to unity, the peak at f_2 is not as sharp as f_1. This results in a short settling time for tracking of the slow sinusoid.

Assuming linear dynamics for the damped nanopositioner, we can achieve approximately zero steady-state tracking error when the feedback controller includes the reference dynamics. In practice, however, the displacement is a nonlinear function of actuation due to the quadratic relationship between force and voltage in an electrostatic MEMS device [16], [22]. Moreover, minor asymmetries of the actuators due to the fabrication tolerances can induce nonlinearities not captured in the system identification. Therefore, higher harmonics of both reference frequencies and their combinations lead to large tracking errors [13], [16]. In Fig. 4(a), d represents disturbances due to

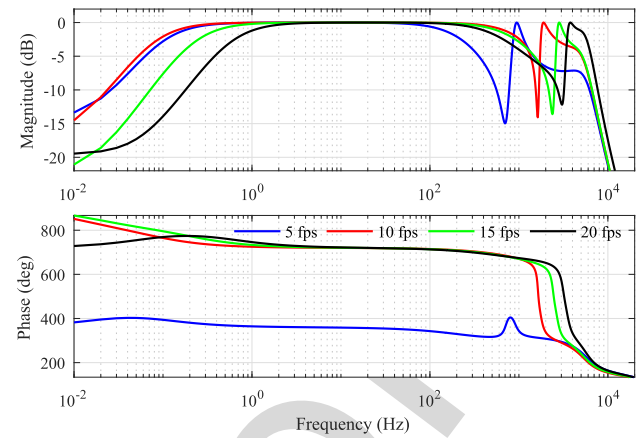

Fig. 5. Simulated frequency response of the closed-loop system with the internal-model-based controller at different frame rates.

unmodeled dynamics and n denotes the sensor noise, which is mainly originated from the piezoresistive elements, amplifiers, and electric components of the readout circuit.

C. Iterative Learning Control

Iterative learning control utilizes information from past experiments to update control action to achieve high-precision tracking of the reference signal in presence of repeating disturbances. We investigate convergence properties of the algorithm and obtain a bound on the asymptotic tracking error. We then design ILC filters that meet the convergence criterion and minimize the ultimate tracking error. In our design, we employ well-established inversion approximation methods to implement the inversion-based learning filter. The control scheme that integrates the ILC with the feedback controller is depicted in Fig. 4(b). For the sake of simplicity, the damping loop is substituted by the damped plant, G_d. For later analysis, the unmodeled disturbance d is projected into the sensor output as d_p. That is

$$d_p = \frac{d}{1 + C_d(z)G(z)}. \tag{9}$$

We assume that disturbances are repeating and iteration invariant, and use the following update law [33], [34]:

$$u_{I,k+1} = Q(z)[u_{I,k} + \alpha L(z)e_k], \quad k \geq 1 \tag{10}$$

where $u_{I,1} = 0$, and $L(z)$ and $Q(z)$ are the learning and robustness filters, respectively. Here, α is the learning gain, and $u_{I,k}$ and e_k denote the ILC control input and the tracking error at the kth iteration, respectively. The tracking results of the kth iteration are available for the update law at the $(k+1)$th iteration. In this approach, $u_{I,k+1}$ is calculated using (10) and augmented to the feedback control input in the current iteration. To guarantee convergence of the ILC algorithm in the iteration domain, tracking error and control inputs must remain bounded

IEEE Proof

in the presence of uncertainties. According to Fig. 4(b), we have

$$\begin{aligned} e_{k+1} &= y_d - y_{k+1} - n_{k+1} \\ u_{k+1} &= u_{C,k+1} + u_{I,k+1} \\ y_{k+1} &= u_{k+1} G_d(z) + d_p. \end{aligned} \tag{11}$$

For simplicity, we discard (z) in the following formulations. To analyze the effect of noise on the steady-state tracking error and convergence, we assume that measurement noise is varying through iterations and uniformly bounded at each iteration, i.e., $|n_k| \leq \delta$. Accordingly, the ILC algorithm converges if the ILC filters are designed such that

$$|Q(1 - \alpha LSG_d)| < 1 \tag{12}$$

and accordingly, the asymptotic error at convergence is bounded by

$$\begin{aligned} e_\infty = \lim_{k\to\infty} |e_k| \leq \frac{|S(1-Q)|}{1-\rho}|y_d - d_p| \\ + \frac{|\alpha SQLSG_d|}{1-\rho}|\delta| + |S||\delta| \end{aligned} \tag{13}$$

where $\rho = Q(1 - \alpha LSG_d)$ and S is the sensitivity function. For the proof and details; see Appendix.

1) Design of Learning Filter L: A number of techniques have been proposed to design the learning filter [24]. According to (22), the learning filter is selected so that

$$L = (SG_d)^{-1}. \tag{14}$$

Therefore, the algorithm converges in one iteration assuming $Q = 1$ and ignoring the effect of noise. The challenge with this technique is the NMP zeros of the plant. NMP zeros are inevitable when the plant is discretized at a certain sampling frequency or when the sensors and actuators are not collocated. To determine stable approximate inversion, well-established techniques such as NMP zeros ignore (NPZ-ignore), zero magnitude error tracking controller (ZMETC), and zero-phase error tracking controller (ZPETC) have been employed [43], [44]. These techniques are straightforward and effective in achieving the desired tracking performance. The NPZ-ignore algorithm ignores a part of system dynamics and, hence, is less accurate than other methods. ZMETC and ZPETC approximate the effect of NMP zero by a stable zero and a stable pole, respectively. The type of the system, the location of NMP zeros, and the nature of the application determine the algorithm most suitable for the approximate inversion [43].

Anticausal filtering [45] or stable inversion [44], [46] are alternatives to inverse approximation methods. They can significantly improve the tracking results. These approaches are based on partitioning the model into two parts consisting of the minimum-phase and NMP zeros. Inversion of the first part is straightforward. However, stable inverse of the second part is anticausal. To perform anticausal filtering, we can replace z with z^{-1} and apply the filter on the time-reversed input sequence.

Here, we explore the performance of ZMETC and anticausal filtering approaches in designing the learning filter. To obtain L using ZMETC, we define $H(z) = S(z)G_d(z)$, i.e.

$$H(z) = \frac{B_s(z)B_u(z)}{A(z)} \tag{15}$$

where $A(z)$ incorporates poles and $B_s(z)$ and $B_u(z)$ include stable and unstable zeros, respectively. Since $H(z)$ is a proper transfer function, we omit the units of delay considered for causal implementation. Here, $B_u(z)$ is a polynomial written as $B_u(z) = b_{u_n} z^n + b_{u_{n-1}} z^{n-1} + \cdots + b_{u_0}$. According to ZMETC, the approximate inverse of $H(z)$ can be obtained by reflecting unstable zeros to stable ones with respect to the unit circle, i.e., $z_{u_i} \to 1/z_{u_i}$. Therefore, $\tilde{H}^{-1}(z)$ can be obtained as

$$\tilde{H}^{-1}(z) = \frac{A(z)}{B_s(z)B_u^\star(z)} \tag{16}$$

where $B_u^\star(z) = b_{u_0} z^n + b_{u_1} z^{n-1} + \cdots + b_{u_n}$. Note that dc gain adjustment is not required since the dc gain remains unchanged.

In anticausal filtering approach [45], $H(z)$ can be factorized into

$$H(z) = H_s(z)H_u(z) \tag{17}$$

where $H_s(z)$ and $H_u(z)$ contain the invertible and noninvertible zeros, respectively. Accordingly, $H_s^{-1}(z)$ is stable and causal, while $H_u^{-1}(z)$ is stable and anticausal. Since the ILC algorithm is applied offline, and the tracking error is available from the previous iteration, we may determine L by anticausal filtering approach. From (10) and (17), we may write

$$w_k(t) = H_s^{-1}(z)e_k(t) \tag{18}$$

then, the anticausal filtering can be implemented by reversing the sequence, $w_k(t)$, and applying the causal filter, i.e.

$$v_k(t) = H_u^{-1}(z^{-1})w_k(N - t). \tag{19}$$

Finally, the filtered output is obtained by reversing $v_k(t)$, i.e., $z_k(t) = v_k(N - t)$. Thus, the ILC control update law in (10) can be rewritten as

$$u_{I,k+1}(z) = Q(z)[u_{I,k}(z) + \alpha z_k], \quad k \geq 1. \tag{20}$$

The anticausal filtering method inverts SG_d implicitly and determines the learning filter. Therefore, the ILC algorithm converges fast and yields smaller tracking error in comparison with the ZMETC, which suffers from approximation error.

2) Design of Robustness Filter Q: According to (13), tracking error approaches zero asymptotically if $Q = 1$ and $|\delta| \approx 0$. In practice, however, $|\delta| \neq 0$ and the Q-filter is typically selected as a low-pass filter to mitigate nonrepeating disturbances and high-frequency noise. The cut-off frequency of Q, on the other hand, should be large enough to include reference frequencies and disturbances. In this case, Q can effectively minimize the deterministic component of the tracking error. It is clear from (13) that in order to minimize the effect of disturbances and noise, we must have $|S(1 - Q)| < 1$ and $|SQ| < 1$. This requires a compromise in designing Q. As discussed in [47], the variance of error at convergence is limited by the variance of iteration varying noise and disturbances. The variance can be reduced by selecting the learning gain as $0 < \alpha \leq 1$. This will ensure that the ILC algorithm will converge with a small tracking error in the

IEEE Proof

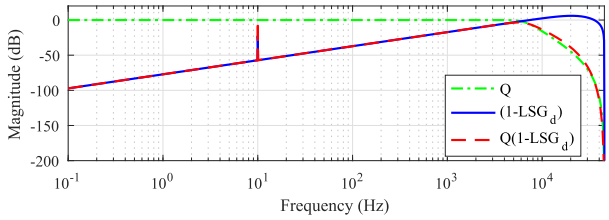

Fig. 6. Magnitude of the low-pass Q-filter, $|1 - LSG_d|$ and $|Q(1 - LSG_d)|$ when the ZMETC technique is employed to design the learning filter for tracking the rosette pattern at 10 fps.

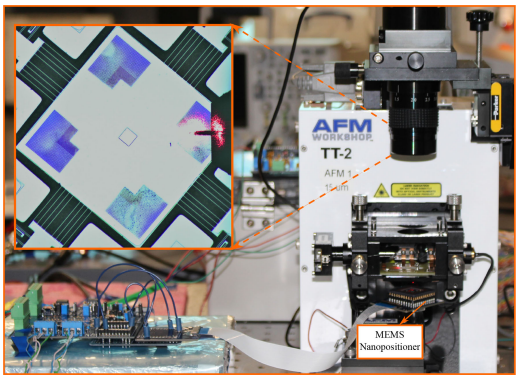

Fig. 7. Experimental setup consists of a MEMS nanopositioner integrated into a commercial AFM. The inset shows the contact-mode cantilever landed on the gold features microfabricated on the scan table [18].

presence of iteration varying noise and disturbances. Decreasing the learning gain will also reduce the convergence rate.

Here, a fourth-order Butterworth filter is used as the Q-filter. The bandwidth of the filter is selected as 5 kHz, 6.5 kHz, 8.5 kHz, and 11 kHz at 5 fps, 10 fps, 15 fps, and 20 fps, respectively. Accordingly, Q-filter ensures the stability and convergence of the ILC algorithm when the ZMETC technique is applied. As shown in Fig. 6, the Q-filter makes $|1 - \alpha LSG_d|$ small at higher frequencies. To avoid any distortion in the output signal due to the phase shift imposed by the filter, a zero-phase filtering is employed using *filtfilt*$(\cdot)$ function in MATLAB.

Since the filter bandwidth is large at high frame rates to encompass higher harmonics, the tracking error may not decrease monotonically due to the high-frequency noise. To address this issue, α is set to 0.7 and 0.5 at 15 fps and 20 fps, respectively, and to unity at 5 fps and 10 fps.

IV. Experiment

To evaluate the performance of the proposed control scheme, we conducted tracking experiments at 5 fps, 10 fps, 15 fps, and 20 fps using a feedback-controlled MEMS nanopositioner, as shown in Fig. 7. In this section, we present the experimental results and discuss the performance of two inversion techniques in tracking the rosette pattern.

A. Implementation

The closed-loop system is implemented in a dSPACE MicroLabBox with a sampling frequency of 90720 Hz. The control signal is amplified to drive the lateral axes of the nanopositioner

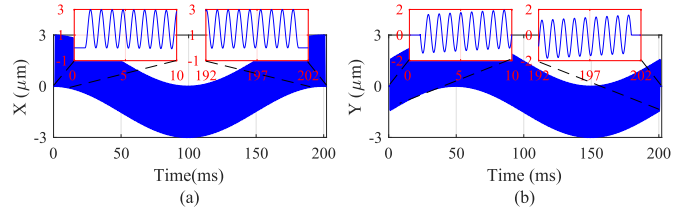

Fig. 8. Reference signals of rosette pattern at 5 fps after zero padding.

and the stage displacement is measured using the sensor output's voltage and predetermined calibration factors. To implement the ILC, we require an interface to communicate between the hardware and the software. ASAM XIL API is a standard utilized in dSPACE to facilitate such communications. Specifically, we used the XIL API model access port to gain access to the SIMULINK model, write into the blocks, and capture signals. We then used the XIL API. NET implementation as a high-level program in a MATLAB script to implement the ILC algorithm, and to read and manipulate the variables online. Initially, the ILC control input is set to zero and the IMBC is employed in the tracking experiment. Then, the experiment is continued iteratively and the desired signals including the tracking error are captured in each iteration to update the ILC control drive signal. The experiment is performed for a specific number of iterations to ensure the convergence of the ILC algorithm. We allow for 15 iterations, although the algorithm converges very fast in practice.

B. Tracking the Rosette Pattern

Since the damped plant is NMP, anticausal learning and filtering may result in transients. To address this issue, we may extend the reference signals by leading and trailing zeros, which we will truncate at the end. The number of zeros N_z is determined such that the imaging rate for single-frame scanning remains almost unchanged. Note that no zero is added to intermediate frames in sequential scanning. Consequently, the extended reference signals, in a single-frame scan, are obtained as

$$x_a(t),\, y_a(t) = \begin{cases} 0 & 0 \le t \le \Delta \\ x(t),\, y(t) & \Delta \le t \le T + \Delta \\ 0 & T + \Delta \le t \le T + 2\Delta \end{cases} \tag{21}$$

where $\Delta = N_z f_s$ and f_s is the sampling frequency. Based on the expected transient time, we select $\Delta = 1/f_1$ with f_1 as described by (2). This extends the scan time to $T + 2\Delta$. Fig. 8 shows the reference signals at 5 fps after zero-padding. In a single-frame scanning, the scan time increases by 1 %, which is negligible.

C. Experimental Results

Initially, we perform closed-loop experiments to track a single frame of the rosette pattern generated by the reference signals in (21). Fig. 9 shows the root-mean-square (RMS) value of tracking error at each iteration and the close-up views indicate the tracking error at convergence. Note that the RMS value of error at the first iteration is corresponding to the IMBC when the ILC is inactive. We observe that the learning algorithm converges quickly,

IEEE Proof

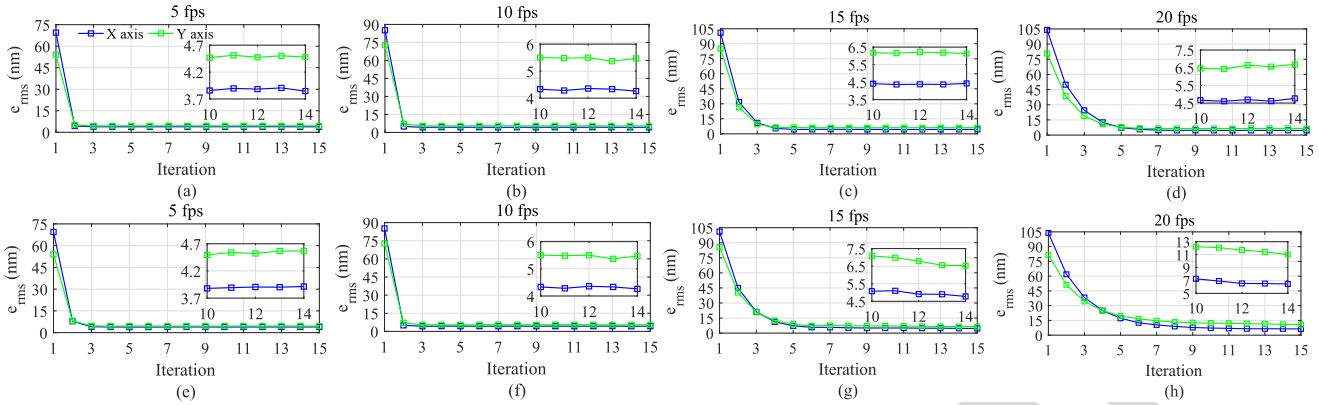

Fig. 9. RMS value of error at each iteration when the anticausal filtering approach (a) to (d) and ZMETC technique (e) to (h) have been employed to determine the learning filter L at (a) and (e) 5 fps, (b) and (f) 10 fps, (c) and (g) 15 fps, (d) and (h) 20 fps.

TABLE II
RMS VALUE OF TRACKING ERROR INCLUDING THE TRANSIENTS AT ALL FRAME RATES

Frame rate (fps)	IMBC		IMBC+ILC			
			Anti-causal		ZMETC	
	e_x(nm)	e_y(nm)	e_x(nm)	e_y(nm)	e_x(nm)	e_y(nm)
5	69.5	54.1	3.9	4.5	3.9	4.5
10	85.1	75.7	4.3	5.4	4.6	5.7
15	101.0	85.2	4.4	6.2	5.0	6.8
20	104.0	80.7	4.7	6.5	6.4	11.9

and tracking error decreases monotonically through iterations with both inversion techniques. At low frame rates, the algorithm converges in less than three iterations, while it takes five to seven iterations for the tracking error to approach the asymptotic value at higher frame rates. It is clear that the learning rate is faster at 5 fps and 10 fps since $\alpha = 1$. Fig. 9(a)–(d) describes a fast convergence rate with the anticausal filtering approach, whereas it takes slightly longer for the algorithm to converge using the ZMETC technique, particularly at higher frame rates; see Fig. 9(e)–(h). It appears that the accuracy of ZMETC degrades at 20 fps as the higher harmonics of the reference frequency lie beyond the bandwidth of the plant resulting in an approximation error. Since single-fame scanning is also performed here, we consider both the transient and steady-state errors in calculation of the RMS values. From experimental results, we observe that the combination of ILC with IMBC properly minimizes the transient and steady-state error at convergence.

Table II presents the RMS value of tracking error with the proposed control scheme. We achieve 90 % improvement with ILC using the anticausal filtering approach. Moreover, the RMS value of tracking error decreases to less than 0.1 % of the scan diameter. Considering the fact that IMBC restricts the sensor noise and bounds the tracking error at the first iteration, integrating the ILC with the IMBC enhances the tracking performance.

To evaluate the efficacy of the proposed control scheme in rejecting the repetitive disturbances, we obtain FFT of the tracking error. Fig. 10 shows FFT of tracking error with anticausal filtering and ZMETC approaches at all frame rates. The closeup views reveal that the ILC precisely removes the higher harmonics not compensated by the IMBC alone. Both inversion techniques yield a good tracking performance, however, assuming identical gains, the anticausal filtering approach outperforms ZMETC at high frame rates; see Fig. 10(h). We observe that at 20 fps fundamental harmonic at f_1 has been removed satisfactorily, however, the second harmonic at 7560 Hz is still dominant in the error.

Fig. 11 depicts the time-domain results for single-frame tracking of the rosette pattern. Because of its effectiveness, here we report the time-domain results with the anticausal filtering only. Note that the padded zeros are truncated from the results. The integration of ILC with IMBC leads to a visible improvement in tracking. We also observe that IMBC leaves a steady-state error in the y-axis when the ILC is off. Although the nanopositioner dynamics are very similar in x and y axes, the y-axis closed-loop system with IMBC cannot follow the low-frequency reference signal in one scan period. Augmenting the tracking controller with integral action may address the issue, but the ILC eliminates the y-axis steady-state error successfully.

As illustrated in the close-up views of Fig. 11, a large peak appears at the beginning and end of y-axis tracking error during single-frame scans. This is due to the nonzero steady-state tracking error and the backward–forward technique used to implement the learning and robustness filters. To prevent the peak of error from affecting single-frame scans, we provide *a priori* learning using the pattern's periodicity. We extend the length of the reference signals by replacing T with $T + 2\epsilon$ in (21). Here, ϵ is selected as $1/f_1$ to cover the transient duration. In this case, the scan time for single-frame scanning increases by less than 2 %. In sequential scanning, consecutive frames are not affected by the error peak meaning that the scan time of successive frames remains unchanged. Therefore, the overall scan time will be $T_f = N_f T + 2\Delta + 2\epsilon$, where N_f is the total number of frames.

Steady-state tracking errors in Table III allows us to compare the performance of proposed control structure with the IMBC during sequential rosette scan assuming that the transient response is disappeared. Combined ILC/IMBC reduces the peak to peak value of steady-state error by 50 % and keeping it below

IEEE Proof

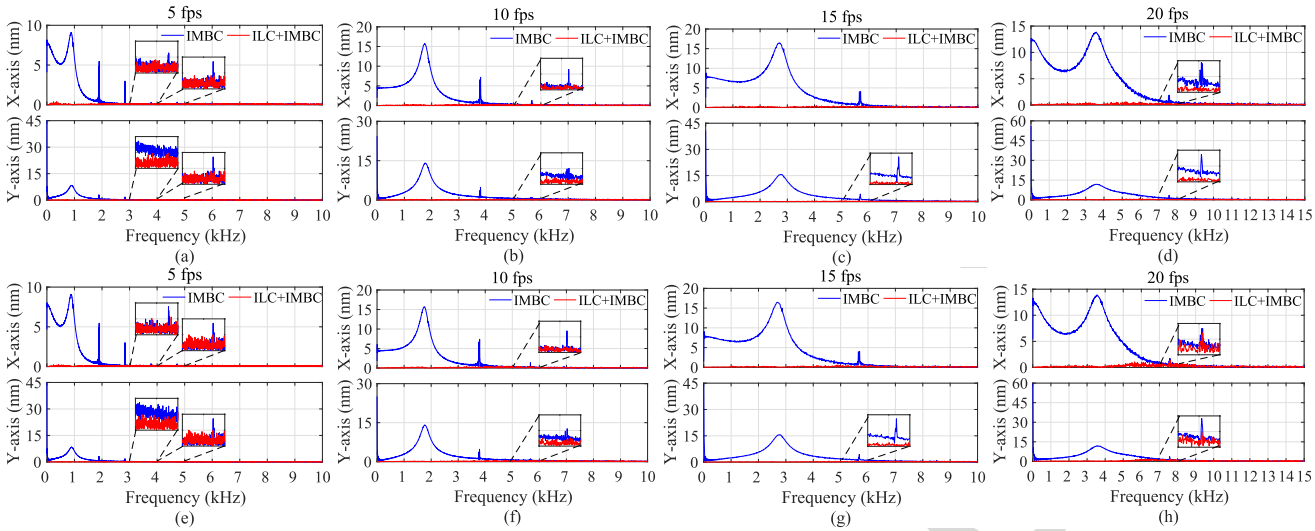

Fig. 10. FFT of tracking error with IMBC and the combination of ILC and IMBC when the anticausal filtering approach (a) to (d) and ZMETC technique (e) to (h) are employed to determine the learning filter (L) at 5 fps, 10 fps, 15 fps, and 20 fps.

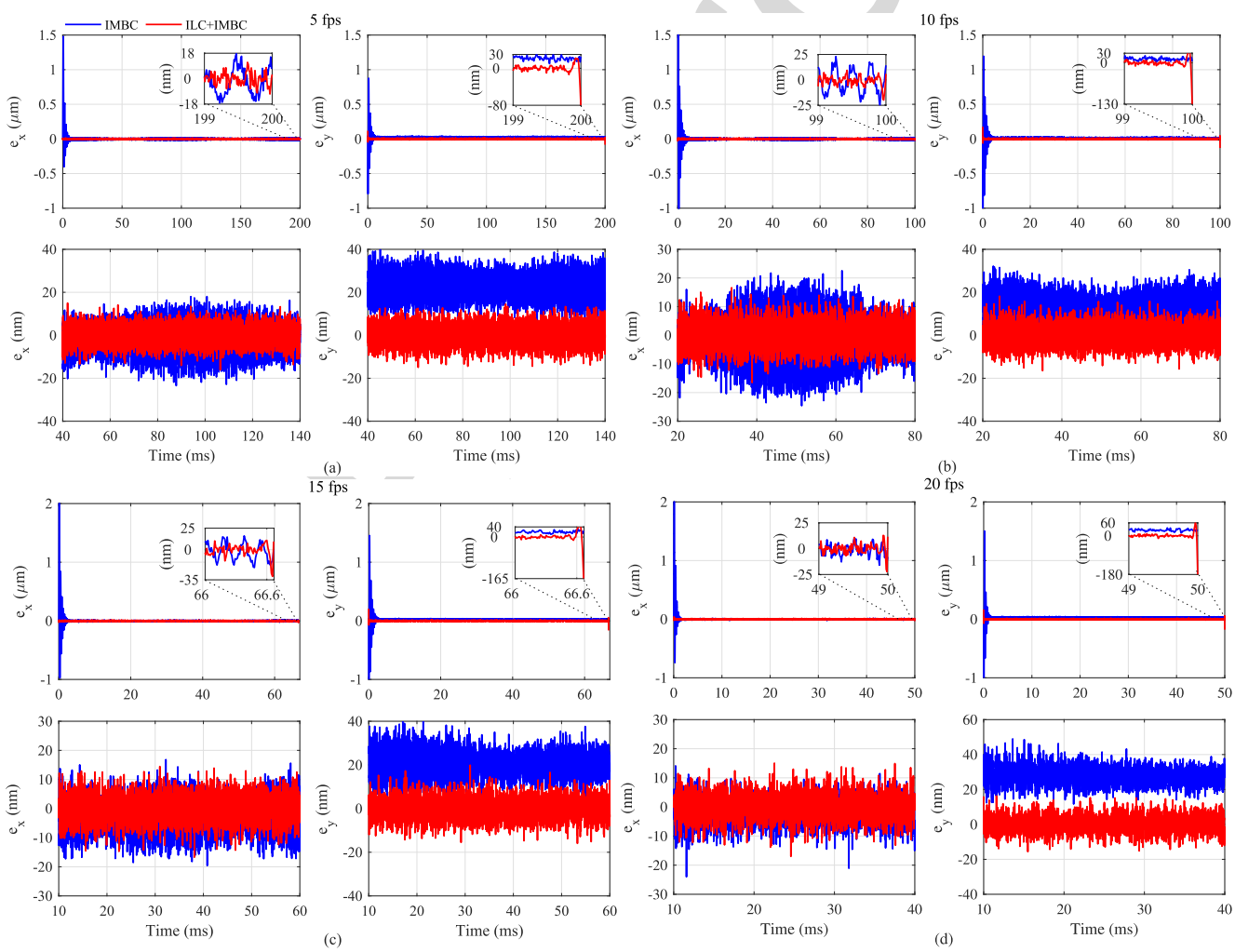

Fig. 11. Time-domain tracking results of single-frame scan at (a) 5 fps, (b) 10 fps, (c) 15 fps, and (d) 20 fps when the anticausal filtering approach is employed to determine the learning filter.

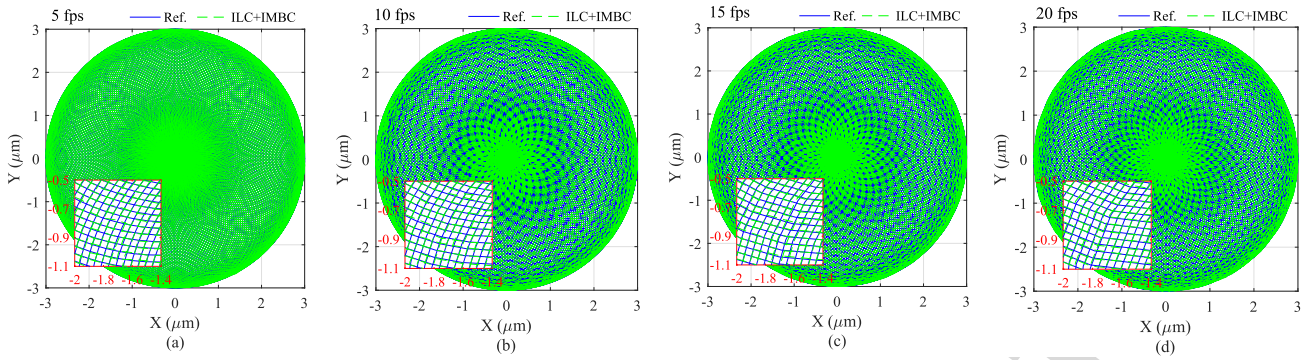

Fig. 12. Reference and actual rosette trajectory at (a) 5 fps, (b) 10 fps, (c) 15 fps, and (d) 20 fps.

TABLE III
RMS VALUE OF STEADY-STATE TRACKING ERROR AT ALL FRAME RATES

Frame rate (fps)	IMBC		IMBC+ILC			
			Anti-causal		ZMETC	
	e_x(nm)	e_y(nm)	e_x(nm)	e_y(nm)	e_x(nm)	e_y(nm)
5	8.2	23.3	3.8	4.2	3.8	4.2
10	9.4	13.8	4.2	4.5	4.5	4.7
15	7.2	21.3	4.3	4.6	4.6	4.8
20	5.7	30.2	4.2	4.8	5.5	7.1

20 nm. In addition, this method improves the x- and y-axis tracking errors by more than 27 % and 79 %, respectively.

As discussed in Section III-C, RMS value of tracking error at convergence is bounded by iteration varying noise and disturbances. According to (13), $e_\infty \leq 2|S||\delta|$ if $Q = 1$, and $L = (SG_d)^{-1}$. Therefore, asymptotic error relies on the sensor output noise fed back to the system. Since IMBC attenuates the high-frequency projected noise, the upper bound on the ultimate error determines the resolution of the displacement sensors. To obtain sensor resolution in open loop and under damping, we recorded sensor output noise for 60 s at a sampling frequency of 62.5 kHz with an antialiasing filter (Stanford Research SR650 low-noise filter) with a cut-off frequency of 15 kHz being used in the path. To reject noise and electrical disturbances, the experiment was performed in a closed metal box. Open-loop RMS value of noise is 2 nm, with the actuators electrically grounded, and it is about 3 nm with the damping loop being active. Asymptotic error obtained with the anticausal filtering approach is bounded by about 4 nm, which is close to the sensor noise floor.

The rosette trajectory and the actual displacement of the stage tracing the rosette pattern are depicted in Fig. 12. Close-up views validate the tracking performance at all frame rates when the ILC is integrated with the internal-model-based controller.

V. AFM IMAGING

To implement rosette scanning with the proposed control scheme, we used an AFMWorkshop TT-AFM. We mounted an MEMS nanopositioner on the AFM 3-DOF positioning mechanism. The MEMS device serves as the scanner in the experiments reported here. As indicated in the inset of Fig. 7, the periodic gold features fabricated on the scan table of the MEMS nanopositioner were used as the sample. Dimensions of the gratings is $4 \times 4 \times 0.5\,\mu\text{m}^3$ with a pitch of 3 μm [5]. Due to the low z-axis bandwidth of the commercial AFM's positioner, we performed the experiments in constant-height contact mode. We used a contact-mode cantilever with a resonance frequency of about 27.8 kHz and stiffness of 0.25 N/m. When the cantilever was landed on the MEMS scan table, we closed the control loop and activated the iterative learning algorithm. X and Y sensor outputs and cantilever deflection were recorded simultaneously to construct 3-D AFM images. Fig. 13 depicts a single-frame of rosette scan at frame rates ranging from 5 to 20 fps, indicating that AFM images have precisely captured the structure of a gold feature.

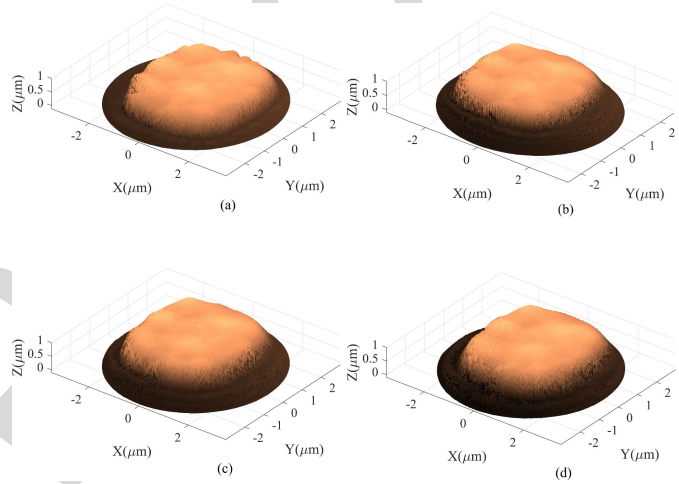

Fig. 13. 3-D AFM images acquired with rosette-scan at (a) 5 fps, (b) 10 fps, (c) 15 fps, and (d) 20 fps on a window size of 6 μm.

We also performed sequential scanning at video rate. To imitate a dynamic process, the AFM positioner was made to raster at 0.2 Hz over a window size of $6 \times 6\,\mu\text{m}^2$ while the MEMS nanopositioner was following the rosette pattern at 20 fps in a scan area with a diameter of 6 μm. Fig. 14 illustrates a series of AFM time-lapsed images that capture the gold feature moving slowly under the cantilever.

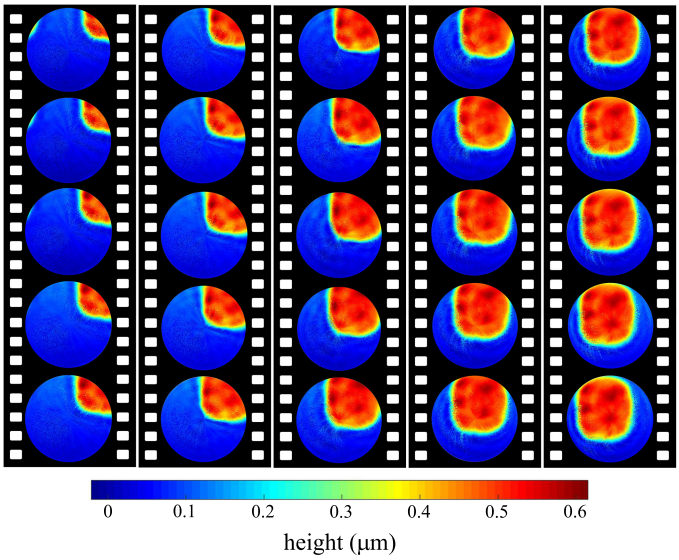

Fig. 14. Series of rosette-scan frames at 20 fps captured in constant-height contact mode on a window size with a diameter of 6 μm.

VI. Conclusion

We demonstrate video-rate rosette scanning by combining an internal-model-based controller with an iterative learning controller. The feedback controller contains an internal model of the reference signals and limits the closed-loop bandwidth to bound the tracking error when the ILC is OFF. The ILC is used to mitigate induced disturbances originating from inherent system nonlinearities. The model-based ILC is designed using well-established inversion techniques. The experimental results validate the efficacy of the control scheme in reducing transient and steady-state tracking errors at several frame rates. We show that this control scheme is suitable for both sequential and single-frame scanning. We acquire successive AFM images of slowly moving gold features at 20 fps in constant-height contact mode. In future works, we will implement the scanning experiment in constant-force contact mode and tapping mode using a high-bandwidth z-axis positioner.

Appendix

According to (11), the tracking error in the $(k+1)$th iteration can be described as

$$e_{k+1} = Q(1-\alpha LSG_d)e_k + S(1-Q)(y_d - d_p) + SQn_k - Sn_{k+1}. \tag{22}$$

Proceeding through iterations, we can derive the relationship between e_{k+1} and e_1 as

$$e_{k+1} = \rho^k e_1 + \sum_{i=0}^{k-1} S(1-Q)(y_d - d_p)\rho^i + \sum_{i=0}^{k-1} SQ\rho^i n_{k-i} - \sum_{i=0}^{k-1} S\rho^i n_{k+1-i} \tag{23}$$

where $\rho = Q(1-\alpha LSG_d)$. By changing the index variable, the last two terms can be combined into one, hence, (23) can be simplified to

$$e_{k+1} = \rho^k e_1 + S(1-Q)(y_d - d_p)\sum_{i=0}^{k-1}\rho^i + SQLSG_d\sum_{i=0}^{k-1}\rho^i n_{k-i} - Sn_{k+1} + \rho^k n_1. \tag{24}$$

Assuming $|n_k| \le \delta$, the upper bound on e_{k+1} is obtained as

$$|e_{k+1}| \le |\rho|^k|e_1| + |S(1-Q)||y_d - d_p|\sum_{i=0}^{k-1}|\rho|^i + |SQLSG_d|\sum_{i=0}^{k-1}|\rho|^i|\delta| - |S||\delta| + |\rho|^k|\delta|. \tag{25}$$

Since the feedback controller is designed to keep the tracking error small at the first iteration, $|e_1|$ is bounded. As a result, (25) implies that the asymptotic error is bounded when $k \to \infty$ if $|\rho| < 1$.

Acknowledgment

Disclaimer: This article was prepared as an account of work sponsored by an agency of the United States Government. Neither the U.S. Government nor any agency thereof, nor any of their employees, makes any warranty, express or implied, or assumes any legal liability or responsibility for the accuracy, completeness, or usefulness of any information, apparatus, product, or process disclosed, or represents that its use would not infringe privately owned rights. Reference herein to any specific commercial product, process, or service by trade name, trademark, manufacturer, or otherwise does not necessarily constitute or imply its endorsement, recommendation, or favoring by the U.S. Government or any agency thereof. The views and opinions of authors expressed herein do not necessarily state or reflect those of the U.S. Government or any agency thereof.

References

[1] N. Kodera and T. Ando, "The path to visualization of walking myosin v by high-speed atomic force microscopy," *Biophys. Rev.*, vol. 6, no. 3, pp. 237–260, 2014.
[2] K. Ariga, T. Mori, and L. K. Shrestha, "Nanoarchitectonics from molecular units to living-creature-like motifs," *Chem. Rec.*, vol. 18, no. 7/8, pp. 676–695, 2018.
[3] Y. Du, J. Pan, and J. H. Choi, "A review on optical imaging of DNA nanostructures and dynamic processes," *Methods Appl. Fluorescence*, vol. 7, no. 1, 2019, Art. no. 012002.
[4] T. Ando, "Directly watching biomolecules in action by high-speed atomic force microscopy," *Biophys. Rev.*, vol. 9, no. 4, pp. 421–429, 2017.
[5] M. Maroufi and S. O. R. Moheimani, "A 2DOF SOI-MEMS nanopositioner with tilted flexure bulk piezoresistive displacement sensors," *IEEE Sensors J.*, vol. 16, no. 7, pp. 1908–1917, Apr. 2016.
[6] S. Watanabe and T. Ando, "High-speed xyz-nanopositioner for scanning ion conductance microscopy," *Appl. Phys. Lett.*, vol. 111, no. 11, 2017, Art. no. 113106.
[7] M. Mahdavi, N. Nikooienejad, and S. O. R. Moheimani, "AFM microcantilever with a collocated AlN sensor-actuator pair: Enabling efficient Q-control for dynamic imaging," *J. Microelectromech. Syst.*, vol. 29, no. 5, pp. 661–668, 2020.

IEEE Proof

[8] A. Bazaei, Y. K. Yong, and S. O. R. Moheimani, "Combining spiral scanning and internal model control for sequential AFM imaging at video rate," *IEEE/ASME Trans. Mechatron.*, vol. 22, no. 1, pp. 371–380, Feb. 2017.

[9] Y. Wu, Y. Fang, X. Ren, and H. Lu, "A wavelet-based AFM fast imaging method with self-tuning scanning frequency," *IEEE Trans. Nanotechnol.*, vol. 16, no. 6, pp. 1088–1098, Nov. 2017.

[10] A. Bazaei, Y. K. Yong, and S. O. R. Moheimani, "High-speed Lissajous-scan atomic force microscopy: Scan pattern planning and control design issues," *Rev. Sci. Instrum.*, vol. 83, no. 6, 2012, Art. no. 063701.

[11] T. Tuma, J. Lygeros, V. Kartik, A. Sebastian, and A. Pantazi, "High-Speed multiresolution scanning probe microscopy based on Lissajous scan trajectories," *Nanotechnology*, vol. 23, no. 18, 2012, Art. no. 185501.

[12] I. A. Mahmood, S. O. R. Moheimani, and B. Bhikkaji, "A new scanning method for fast atomic force microscopy," *IEEE Trans. Nanotechnol.*, vol. 10, no. 2, pp. 203–216, Mar. 2011.

[13] A. Bazaei, M. Maroufi, A. G. Fowler, and S. O. R. Moheimani, "Internal model control for spiral trajectory tracking with MEMS AFM scanners," *IEEE Trans. Control Syst. Technol.*, vol. 24, no. 5, pp. 1717–1728, Sep. 2016.

[14] D. Ziegler, T. R. Meyer, A. Amrein, A. L. Bertozzi, and P. D. Ashby, "Ideal scan path for high-speed atomic force microscopy," *IEEE/ASME Trans. Mechatron.*, vol. 22, no. 1, pp. 381–391, Feb. 2017.

[15] Y. K. Yong, S. O. R. Moheimani, and I. R. Petersen, "High-speed cycloid-scan atomic force microscopy," *Nanotechnology*, vol. 21, no. 36, 2010, Art. no. 365503.

[16] N. Nikooienejad, A. Alipour, M. Maroufi, and S. O. R. Moheimani, "Video-rate non-raster AFM imaging with cycloid trajectory," *IEEE Trans. Control Syst. Technol.*, vol. 28, no. 2, pp. 436–447, Mar. 2020.

[17] M. Shibata, H. Watanabe, T. Uchihashi, T. Ando, and R. Yasuda, "High-speed atomic force microscopy imaging of live mammalian cells," *Biophys. Physicobiol.*, vol. 14, pp. 127–135, 2017.

[18] N. Nikooienejad, M. Maroufi, and S. O. R. Moheimani, "Rosette-scan video-rate atomic force microscopy: Trajectory patterning and control design," *Rev. Sci. Instrum.*, vol. 90, no. 7, 2019, Art. no. 073702.

[19] M. S. Rana, H. R. Pota, and I. R. Petersen, "Spiral scanning with improved control for faster imaging of AFM," *IEEE Trans. Nanotechnol.*, vol. 13, no. 3, pp. 541–550, May 2014.

[20] A. Bazaei, M. Maroufi, and S. R. Moheimani, "Tracking control of constant-linear-velocity spiral reference by LQG method," *IFAC-PapersOnLine*, vol. 50, no. 1, pp. 15568–15573, 2017.

[21] M. G. Ruppert, M. Maroufi, A. Bazaei, and S. R. Moheimani, "Kalman filter enabled high-speed control of a MEMS nanopositioner," *IFAC-PapersOnLine*, vol. 50, no. 1, pp. 15554–15560, 2017.

[22] M. Maroufi, A. G. Fowler, A. Bazaei, and S. O. R. Moheimani, "High-stroke silicon-on-insulator MEMS nanopositioner: Control design for non-raster scan atomic force microscopy," *Rev. Sci. Instrum.*, vol. 86, no. 2, 2015, Art. no. 023705.

[23] S. Arimoto, S. Kawamura, and F. Miyazaki, "Bettering operation of robots by learning," *J. Robot. Syst.*, vol. 1, no. 2, pp. 123–140, 1984.

[24] D. A. Bristow, M. Tharayil, and A. G. Alleyne, "A survey of iterative learning control," *IEEE Control Syst. Mag.*, vol. 26, no. 3, pp. 96–114, Jun. 2006.

[25] F. Boeren, A. Bareja, T. Kok, and T. Oomen, "Frequency-domain ILC approach for repeating and varying tasks: With application to semiconductor bonding equipment," *IEEE/ASME Trans. Mechatron.*, vol. 21, no. 6, pp. 2716–2727, Dec. 2016.

[26] Z. Wang, C. P. Pannier, K. Barton, and D. J. Hoelzle, "Application of robust monotonically convergent spatial iterative learning control to microscale additive manufacturing," *Mechatronics*, vol. 56, pp. 157–165, 2018.

[27] Q. Zhu, F. Song, J. Xu, and Y. Liu, "An internal model based iterative learning control for wafer scanner systems," *IEEE/ASME Trans. Mechatron.*, vol. 24, no. 5, pp. 2073–2084, Oct. 2019.

[28] J. van Zundert, J. Bolder, and T. Oomen, "Optimality and flexibility in iterative learning control for varying tasks," *Automatica*, vol. 67, pp. 295–302, 2016.

[29] V. Dao and S. Chen, "Helical contouring control with online iterative learning control," in *Proc. IEEE/ASME Int. Conf. Adv. Intell. Mechatron.*, 2018, pp. 599–603.

[30] Y. Chen, K. L. Moore, J. Yu, and T. Zhang, "Iterative learning control and repetitive control in hard disk drive industry—A tutorial," in *Proc. IEEE Conf. Decis. Control*, 2006, pp. 2338–2351.

[31] K. K. Leang and S. Devasia, "Design of hysteresis-compensating iterative learning control for piezo-positioners: Application to atomic force microscopes," *Mechatronics*, vol. 16, no. 3, pp. 141–158, 2006.

[32] Y. Wu and Q. Zou, "Iterative control approach to compensate for both the hysteresis and the dynamics effects of piezo actuators," *IEEE Trans. Control Syst. Technol.*, vol. 15, no. 5, pp. 936–944, Sep. 2007.

[33] Y. Wu, Q. Zou, and C. Su, "A current cycle feedback iterative learning control approach for AFM imaging," *IEEE Trans. Nanotechnol.*, vol. 8, no. 4, pp. 515–527, Jul. 2009.

[34] D. Huang, J. Xu, V. Venkataramanan, and T. C. T. Huynh, "High-performance tracking of piezoelectric positioning stage using current-cycle iterative learning control with gain scheduling," *IEEE Trans. Ind. Electron.*, vol. 61, no. 2, pp. 1085–1098, Feb. 2014.

[35] Y. Jian, D. Huang, J. Liu, and D. Min, "High-precision tracking of piezoelectric actuator using iterative learning control and direct inverse compensation of hysteresis," *IEEE Trans. Ind. Electron.*, vol. 66, no. 1, pp. 368–377, Jan. 2019.

[36] S. Xie and J. Ren, "High-speed AFM imaging via iterative learning-based model predictive control," *Mechatronics*, vol. 57, pp. 86–94, 2019.

[37] M. S. de Oliveira and A. T. Salton, "Iterative learning control for spiral scanning patterns in atomic force microscopy," in *Intelligent Robotics and Applications*. Berlin, Germany: Springer, 2018, pp. 389–399.

[38] J. Ling, Z. Feng, M. Ming, Z. Guo, and X. Xiao, "Integrating damping control with iterative learning control for fast and precise scanning of nanopositioners: A TITO design*," in *Proc. Int. Conf. Adv. Robot. Mechatron.*, 2018, pp. 183–188.

[39] H. Xie, Y. Wen, X. Shen, H. Zhang, and L. Sun, "High-speed AFM imaging of nanopositioning stages using H_∞ and iterative learning control," *IEEE Trans. Ind. Electron.*, vol. 67, no. 3, pp. 2430–2439, Mar. 2020.

[40] N. Nikooienejad, M. Maroufi, and S. O. R. Moheimani, "Iterative learning control for high-speed rosette trajectory tracking," in *Proc. IEEE Conf. Decis. Control*, 2019, pp. 6832–6837.

[41] M. Maroufi, A. Bazaei, A. Mohammadi, and S. O. R. Moheimani, "Tilted beam piezoresistive displacement sensor: Design, modeling, and characterization," *J. Microelectromech. Syst.*, vol. 24, no. 5, pp. 1594–1605, 2015.

[42] B. Francis and W. Wonham, "The internal model principle of control theory," *Automatica*, vol. 12, no. 5, pp. 457–465, 1976.

[43] J. Butterworth, L. Pao, and D. Abramovitch, "Analysis and comparison of three discrete-time feedforward model-inverse control techniques for nonminimum-phase systems," *Mechatronics*, vol. 22, no. 5, pp. 577–587, 2012.

[44] J. van Zundert and T. Oomen, "On inversion-based approaches for feed-forward and ILC," *Mechatronics*, vol. 50, pp. 282–291, 2018.

[45] O. Markusson, H. Hjalmarsson, and M. Norrlof, "Iterative learning control of nonlinear non-minimum phase systems and its application to system and model inversion," in *Proc. IEEE Conf. Decis. Control*, 2001, vol. 5, pp. 4481–4482.

[46] R. de Rozario, A. J. Fleming, and T. Oomen, "Finite-time learning control using frequency response data with application to a nanopositioning stage," *IEEE/ASME Trans. Mechatron.*, vol. 24, no. 5, pp. 2085–2096, Oct. 2019.

[47] M. Butcher, A. Karimi, and R. Longchamp, "A statistical analysis of certain iterative learning control algorithms," *Int. J. Control*, vol. 81, no. 1, pp. 156–166, 2008.

Nastaran Nikooienejad received the B.Sc. and M.Sc. degrees in electrical engineering from Shiraz University and Amirkabir University of Technology, in 2006 and 2009, respectively. She is currently working toward the Ph.D. degree in electrical engineering from the University of Texas at Dallas.

Her research interests include high-precision control of MEMS devices, video-rate atomic force microscopy, and signal and image processing.

IEEE Proof

Mohammad Maroufi received the double B.Sc. degrees in mechanical engineering and applied physics and the master's degree in mechatronics from the Amirkabir University of Technology (Tehran Polytechnic), Tehran, Iran, in 2008 and 2011, respectively, and the Ph.D. degree in electrical engineering from the University of Newcastle, Callaghan, NSW, Australia, in 2015.

From 2015 to 2019, he continued his career as the Research Associate and then Research Scientist Postdoctoral appointments with the University of Texas at Dallas, Richardson, TX, USA. He is currently a Motion Sensing Hardware Engineer with the Consumer Electronics Industry. His research interests include development of ultrahigh-precision mechatronic systems and design and control of MEMS nanopositioners.

S. O. Reza Moheimani (Fellow, IEEE) received the Ph.D. in electrical engineering from the University of New South Wales, Australia, in 1996.

He currently holds the James Von Ehr Distinguished Chair in Science and Technology with the Department of Systems Engineering, University of Texas at Dallas with appointments in Electrical and Computer Engineering and Mechanical Engineering Departments. His current research interests include applications of control and estimation in high-precision mechatronic systems, high-speed scanning probe microscopy and atomically precise manufacturing of solid-state quantum devices.

Dr. Moheimani is a Fellow of IEEE, IFAC and the Institute of Physics, U.K. He is a recipient of several awards, including IFAC Nathaniel B. Nichols Medal and IEEE Control Systems Technology Award. He is the Editor-in-Chief of Mechatronics.

IEEE Proof

Iterative Learning Control for Video-Rate Atomic Force Microscopy

Nastaran Nikooienejad, Mohammad Maroufi, and S. O. Reza Moheimani, *Fellow, IEEE*

***Abstract*—We present a control scheme for video-rate atomic force microscopy with rosette pattern. The controller structure involves a feedback internal-model-based controller and a feedforward iterative learning controller. The iterative learning controller is designed to improve tracking performance of the feedback-controlled scanner by rejecting the repetitive disturbances arising from the system nonlinearities. We investigate the performance of two inversion techniques for constructing the learning filter. We conduct tracking experiments using a two-degree-of-freedom microelectromechanical system (MEMS) nanopositioner at frame rates ranging from 5 to 20 frames per second. The results reveal that the algorithm converges rapidly and the iterative learning controller significantly reduces both the transient and steady-state tracking errors. We acquire and report a series of high-resolution time-lapsed video-rate AFM images with the rosette pattern.**

***Index Terms*—Internal model principle, iterative learning control (ILC), microelectromechanical system (MEMS) nanopositioner, nonraster scanning, rosette pattern, video-rate atomic force microscopy (AFM).**

I. Introduction

VIDEO-RATE atomic force microscopy (AFM) has enabled direct visualization of dynamic processes at extremely high resolutions [1]–[4]. Until recently, it could take up to several minutes to capture a high-resolution image with an AFM due to limitations arising from the highly resonant nature of AFMs and the conventional method of scanning, i.e., rastering. There have been significant research efforts aimed at improving the functionality of AFM for high-speed imaging [5]–[9]. In particular, nonraster scan patterns have been proposed to circumvent the drawbacks due to rastering by generating smooth trajectories that are easier to navigate for a mechanical scanner. Although nonraster scan patterns such as Lissajous [10], [11], spiral [12]–[14], and cycloid [15], [16] have been successfully implemented, more research is needed to establish their performance in video-rate sequential imaging for applications that require capturing continuous interactions with nanostructures [17].

In sequential spiral and cycloid scans, back and forth motions of the scanner impose sharp transitions at the periphery of scan area, deteriorating the resulting AFM images [8], [16]. To address common issues with sequential scanning AFM methods, we recently proposed a novel nonraster method based on the rosette pattern [18]. This repetitive pattern can be used to acquire time-lapsed AFM images without the need for undesirable back and forth motions of the positioner.

A number of control design techniques such as model predictive control [19], linear quadratic Gaussian control [20], Kalman-filter-based control [21], and internal-model-based control [13] have been successfully applied to nonraster scanning problems. In particular, promising results have been obtained with the IMBC [10], [13], [16], [22]. This controller achieves asymptotic zero steady-state tracking error by incorporating an internal model of reference signals and disturbances. However, this method requires accurate identification of disturbances, predominantly arising from unmodeled system nonlinearities [10], [13], [16], [22]. Due to the sinusoidal nature of reference signals in nonraster scan patterns, such disturbances typically contain higher harmonics of reference frequencies. Consequently, the controller needs to be redesigned when the reference frequency is changed.

Employing a learning procedure enables us to eliminate the effect of repeating disturbances without the need for performing *a priori* identification experiments and subsequent design of a new controller. The method known as iterative learning control (ILC) [23], [24] was initially proposed for dealing with robotic systems that perform repetitive tasks. Recent research has concentrated on improving the performance of such systems and their applications to other systems that involve performing repetitive tasks [25]–[30].

More recently, ILC has found applications in lateral and vertical nanopositioning for AFM [31]–[38]. In [31] and [32], an iterative learning controller is designed for a piezo-based positioner and applied to an AFM system to decrease the tracking error arising from hysteresis and vibrations. In [33], a current-cycle-feedback ILC is integrated with an H_∞ feedback controller and applied to the z-axis positioner of AFM to achieve high-precision tracking of sample profiles. Integration of ILC

Manuscript received November 18, 2019; revised March 23, 2020 and August 20, 2020; accepted September 26, 2020. Recommended by Technical Editor G. Clayton and Senior Editor X. Tan. This work was supported in part by the University of Texas at Dallas and in part by the U.S. Department of Energy's Office of Energy Efficiency and Renewable Energy (EERE) under the Advanced Manufacturing Office Award DE-EE0008322. *(Corresponding author: S. O. Reza Moheimani.)*

Nastaran Nikooienejad and S. O. Reza Moheimani are with the Erik Jonsson School of Engineering and Computer Science, The University of Texas at Dallas, Richardson, TX 75080 USA (e-mail: nastaran.nikooienejad@utdallas.edu; reza.moheimani@utdallas.edu).

Mohammad Maroufi was with the Erik Jonsson School of Engineering and Computer Science, The University of Texas at Dallas, Richardson, TX 75080 USA. He resides in San Jose, CA 95126 USA. (e-mail: mohammad.maroufi@utdallas.edu).

Color versions of one or more of the figures in this article are available online at https://ieeexplore.ieee.org.

Digital Object Identifier 10.1109/TMECH.2020.3032565

1083-4435 © 2020 IEEE. Personal use is permitted, but republication/redistribution requires IEEE permission.
See https://www.ieee.org/publications/rights/index.html for more information.

IEEE Proof

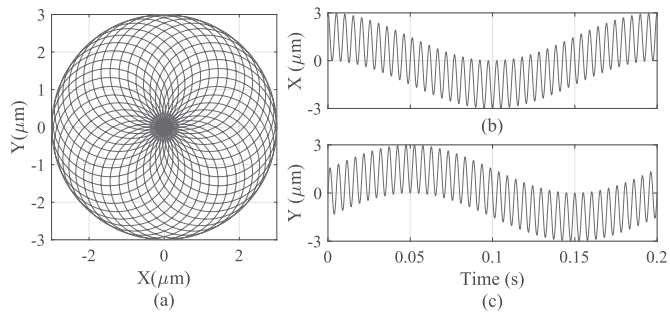

Fig. 1. (a) Rosette pattern when $R = 3\,\mu$m, $P = 250$ nm and $T = 0.2$ s. (b) and (c) Reference signals in x and y axes that generate the rosette pattern in (a).

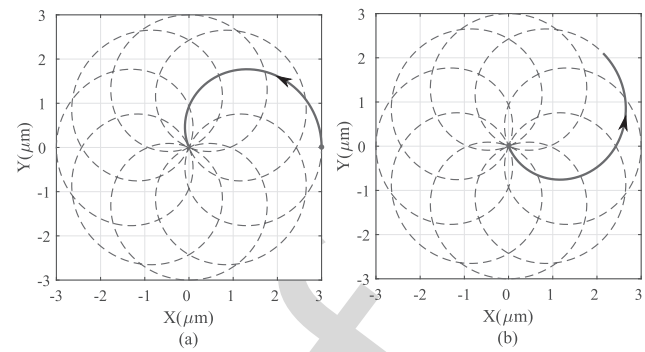

Fig. 2. (a) Rosette pattern generated from (4) starting at $(x, y) = (3, 0)$. (b) Rosette pattern generated from (7) starting at $(x, y) = (0, 0)$. The red dot (•) indicates the starting point.

with model predictive control is reported in [36] to improve the convergence rate in z-axis control of AFM. For lateral scanning, Ling *et al.* [38] propose a control scheme consisting of an integral resonant control and a PID-type ILC to augment the damping of a piezo-actuated nanopositioner. The ILC and model-based H_∞ control are combined in [39] to improve the quality of imaging in sinusoidal scanning at 80 Hz. In [37], the ILC is applied as an add-on control loop to enhance the performance of an existing PI controller for tracking an optimal spiral pattern at high frame rates.

The rest of this article is organized as follows. Section II illustrates sequential scanning with a novel nonraster scan pattern. In Section III, ILC-based control system is developed by integrating the ILC with an internal-model-based controller (IMBC) to achieve robustness against uncertainties and repetitive disturbances. In Section IV, the efficacy of the proposed approach is experimentally investigated by applying to a two-degree-of-freedom (2-DOF) microelectromechanical system (MEMS) nanopositioner. Performing high-resolution video-rate AFM imaging with a novel nonraster scan pattern is presented in Section V, and Section VI concludes this article.

To the best of the authors' knowledge, this is the first successful application of ILC to video-rate nonraster AFM imaging.

II. Sequential Scanning

To implement sequential scanning, we employ the rosette pattern [18]. In this method, the nanopositioner traverses a circular-shaped area continuously without the need for back and forth motion required in conventional raster scanning. Fig. 1 illustrates a rosette pattern and the corresponding reference signals consisting of the sum of two sinusoids with different frequencies but identical amplitudes. We can determine the amplitude and frequencies of the reference signals from the radius of the scan area (R), resolution (P), and the scan period (T). According to the design procedure described in [18], the number of petals in the rosette pattern is obtained as

$$2N = \text{Round}\left(\frac{R\pi}{P}\right). \tag{1}$$

We select N as an even integer to ensure that the pattern would cover the entire scan area. For instance, the rosette pattern in Fig. 1(a) consists of 38 overlapping petals intersecting each other at several points. For larger values of N, the number of petals increases, and high-resolution scanning is achieved.

Reference frequencies in a rosette pattern are determined from

$$\begin{aligned} f_1 &= (1+n)f \\ f_2 &= (1-n)f \end{aligned} \tag{2}$$

where f is the fundamental scan frequency, and n is selected as a rational number expressed by

$$n = \frac{N}{N+1}, \quad N \in \{2, 4, \ldots, 2\,k, \ldots\}. \tag{3}$$

Finally, the lateral axes of the nanopositioner are actuated by the following references:

$$\begin{aligned} x(t) &= \frac{R}{2}\left[\cos(2\pi f_1 t) + \cos(2\pi f_2 t)\right] \\ y(t) &= \frac{R}{2}\left[\sin(2\pi f_1 t) + \sin(2\pi f_2 t)\right]. \end{aligned} \tag{4}$$

From (2) and (4), the total scan time with the rosette pattern is obtained as

$$T = \frac{N+1}{f}. \tag{5}$$

Fig. 1(b) and (c) depicts $x(t)$ and $y(t)$ for a rosette pattern with $R = 3\,\mu$m, $P = 250$ nm, and $T = 0.2$ s.

To trace the rosette pattern, the starting point is at $(x, y) = (R, 0)$ according to (4). Then, the pattern repeats itself continuously from that point on; see Fig. 2(a). Since the nanopositioner rests at $(x, y) = (0, 0)$ when in equilibrium, we need to move it to the starting point each time it returns to the initial position. One approach is to multiply the references with a trapezoidal signal to move the positioner to the starting point linearly and decrease the reference amplitude to zero after sequential scanning is completed [40].

An alternative is to take advantage of the rosette pattern's periodicity by adding a constant phase to the reference signals in both axes to force the pattern to start at $(x, y) = (0, 0)$, as shown in Fig. 2(b). The phase shift is equivalent to the time duration required for the rosette to traverse half of a petal. As explained in [18], it takes $\frac{1}{2nf}$ (s) to draw a petal. Hence, the

IEEE Proof

phase shift corresponding to half of this duration is obtained as

$$\phi_1 = \frac{\pi(1+n)}{2n}, \quad \phi_2 = \frac{\pi(1-n)}{2n} \tag{6}$$

for the first and the second sinusoid in the reference signals. Consequently, reference signals that generate a rosette pattern starting at $(x, y) = (0, 0)$ are

$$\begin{aligned} x(t) &= \frac{R}{2}\left[\cos(2\pi f_1 t + \phi_1) + \cos(2\pi f_2 t + \phi_2)\right] \\ y(t) &= \frac{R}{2}\left[\sin(2\pi f_1 t + \phi_1) + \sin(2\pi f_2 t + \phi_2)\right]. \end{aligned} \tag{7}$$

In this article, the nanopositioner is driven to follow the reference signals in (7) to scan a circular-shaped area with a diameter of $6\,\mu$m and a scan resolution of 50 nm at frame rates ranging from 5 to 20 fps. We employ the ILC method discussed in the following section combined with a feedback controller to improve the tracking performance of the nanopositioner.

III. Control Design

Although inversion based techniques are intuitive and can be easily implemented, their efficacy depends on the accuracy of the estimated plant dynamics. Iterative techniques such as ILC improve tracking in the presence of unmodeled system nonlinearities through learning from past experiences. However, being an open-loop controller, the ILC cannot guarantee robustness against stochastic nonrepeating disturbances. This issue can be addressed by combining the ILC with a feedback controller. The feedback controller should be capable of tracking the reference signals at high speed and, given the sinusoidal nature of those signals, it should be able to achieve this objective with low bandwidth. The internal-model-based controller (IMBC) is well-suited for this purpose. By limiting closed-loop bandwidth, this controller minimizes the effect of projected sensor noise on positioning resolution.

Despite the many advantages of IMBC, this controller cannot deal with exogenous disturbances and system nonlinearities. To achieve robustness, a model of disturbances needs to be included in the feedback controller. This requires extensive experiments and typically results in a very high-order controller [13].

In this section, we design the IMBC to track the fundamental frequencies of the reference signals and achieve acceptable performance and good stability margins. Then, we proceed to design the ILC and integrate it with IMBC. We investigate the convergence properties of this control scheme to ensure satisfactory results. The proposed control scheme is suitable for both single-frame and sequential AFM imaging.

A. MEMS Nanopositioner

To experimentally investigate the controller's performance, we employ a 2-DOF MEMS nanopositioner whose design and characterization are described in detail in [5] and [41]. In this device, four electrostatic actuators move the stage bidirectionally along its lateral axes and on-chip bulk piezoresistive sensors measure the stage displacement with nanoscale precision.

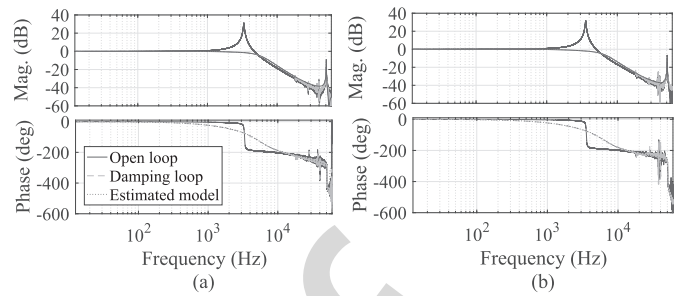

Fig. 3. Frequency response of the nanopositioner from the actuation voltage to sensor output in open loop, with the damping loop and the estimated model of the damped system in (a) x axis and (b) y axis.

Sensor calibration factors are obtained as $0.2176\,\mathrm{V}/\mu\mathrm{m}$ and $0.1958\,\mathrm{V}/\mu\mathrm{m}$ for the x and y axes, respectively.

Frequency response of the scanner is measured by applying a wide-band chirp signal and recording the sensor output using a fast Fourier transform (FFT) analyzer. Fundamental resonant frequencies of the scanner are at 3.34 kHz and 3.57 kHz for x and y axes, respectively; see Fig. 3. As described in [16], [20], and [21], we use an analog controller to add damping to this highly resonant system resulting in a closed-loop bandwidth of approximately 4.5 kHz. We then identify a dynamical model of the damped system that is a good fit up to a bandwidth of 60 kHz; see Fig. 3. In order to design the ILC, the estimated model is then discretized using a zero-order hold at a sampling frequency of 90720 Hz. This results in a nonminimum phase (NMP) model with a pair of complex zeros outside the unit circle at $0.98 \pm j3.25$ and $0.54 \pm j7.11$ for x and y axes, respectively.

B. Internal-Model-Based Controller

According to the internal model principle, steady-state tracking error asymptotically tends to zero when the controller includes an internal model of the reference signals [42]. Knowing the reference *a priori*, we can design the controller by including roots of reference generating polynomial in the controller denominator and tuning the gain and zeros to place closed-loop poles at desirable locations in order to attain acceptable tracking and stability margins. Since reference signals for rosette pattern scanning consist of pure sinusoids, the controller must contain pure imaginary poles at those reference frequencies. The control loop for one axis is shown in Fig. 4(a) where C_d and C denote the damping and internal-model-based controllers, respectively. Taking Laplace transform of reference signals in (7) and assuming a proper controller with pure imaginary poles at $\pm j\omega_1$ and $\pm j\omega_2$, we obtain

$$\begin{aligned} C_x &= \frac{a_4\, s^4 + a_3\, s^3 + a_2\, s^2 + a_1 s + a_0}{(s^2+\omega_1^2)(s^2+\omega_2^2)} \\ C_y &= \frac{b_4\, s^4 + b_3\, s^3 + b_2\, s^2 + b_1 s + b_0}{(s^2+\omega_1^2)(s^2+\omega_2^2)}. \end{aligned} \tag{8}$$

Polynomial coefficients in (8) are determined based on the desired closed-loop poles and stability margins. We tune controller zeros to set the magnitude of the closed-loop response to

IEEE Proof

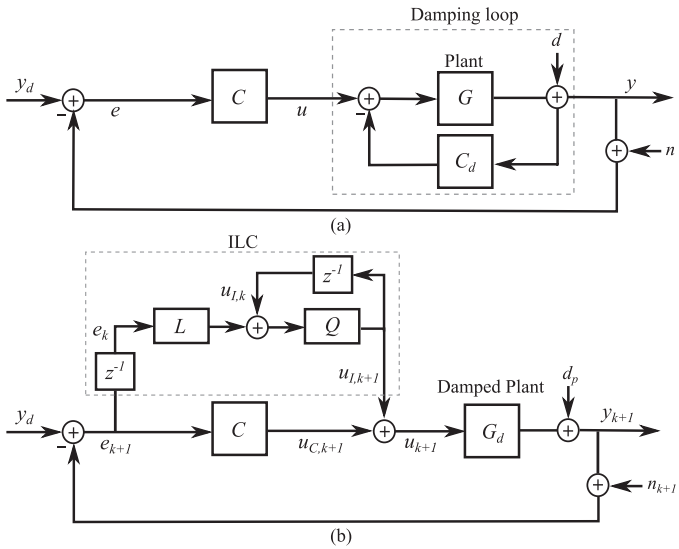

Fig. 4. (a) Control scheme with damping loop (C_d) and feedback controller (C). (b) Control scheme with the combination of iterative learning controller and feedback controller. The damped plant is modeled as G_d and the projected unmodeled disturbance is denoted by d_p. Here, L and Q are the learning and robustness filters in ILC, and z^{-1} indicates a shift in the iteration domain.

TABLE I
REFERENCE FREQUENCIES AND STABILITY MARGINS AT ALL FRAME RATES

Frame Rate	f_1 (Hz)	f_2 (Hz)		GM (dB)	PM (deg)
5 fps	945	5	C_x	17.2	100
			C_y	17.8	101
10 fps	1890	10	C_x	13.6	77.9
			C_y	14.7	80.1
15 fps	2835	15	C_x	14.5	75.8
			C_y	15.3	79.2
20 fps	3780	20	C_x	13.7	67.2
			C_y	12.9	68.9

unity at the desired reference frequencies. In Table I, we state the reference frequencies and stability margins for each frame rate. Simulated frequency responses of the x-axis closed-loop system at various frame rates are depicted in Fig. 5. The y-axis responses are similar. Although the closed-loop response at f_1 and f_2 is set to unity, the peak at f_2 is not as sharp as f_1. This results in a short settling time for tracking of the slow sinusoid.

Assuming linear dynamics for the damped nanopositioner, we can achieve approximately zero steady-state tracking error when the feedback controller includes the reference dynamics. In practice, however, the displacement is a nonlinear function of actuation due to the quadratic relationship between force and voltage in an electrostatic MEMS device [16], [22]. Moreover, minor asymmetries of the actuators due to the fabrication tolerances can induce nonlinearities not captured in the system identification. Therefore, higher harmonics of both reference frequencies and their combinations lead to large tracking errors [13], [16]. In Fig. 4(a), d represents disturbances due to

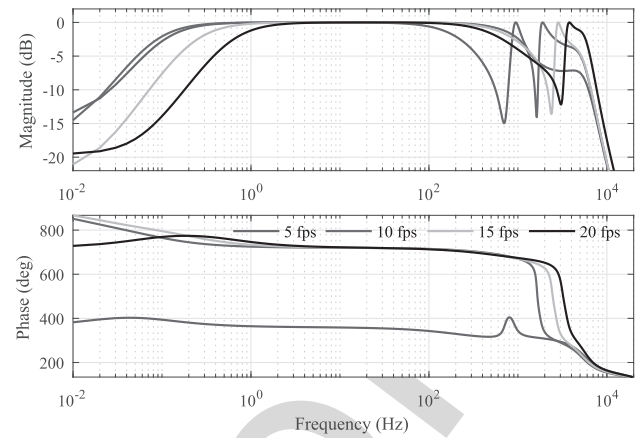

Fig. 5. Simulated frequency response of the closed-loop system with the internal-model-based controller at different frame rates.

unmodeled dynamics and n denotes the sensor noise, which is mainly originated from the piezoresistive elements, amplifiers, and electric components of the readout circuit.

C. Iterative Learning Control

Iterative learning control utilizes information from past experiments to update control action to achieve high-precision tracking of the reference signal in presence of repeating disturbances. We investigate convergence properties of the algorithm and obtain a bound on the asymptotic tracking error. We then design ILC filters that meet the convergence criterion and minimize the ultimate tracking error. In our design, we employ well-established inversion approximation methods to implement the inversion-based learning filter. The control scheme that integrates the ILC with the feedback controller is depicted in Fig. 4(b). For the sake of simplicity, the damping loop is substituted by the damped plant, G_d. For later analysis, the unmodeled disturbance d is projected into the sensor output as d_p. That is

$$d_p = \frac{d}{1 + C_d(z)G(z)}. \tag{9}$$

We assume that disturbances are repeating and iteration invariant, and use the following update law [33], [34]:

$$u_{I,k+1} = Q(z)[u_{I,k} + \alpha L(z)e_k], \quad k \geq 1 \tag{10}$$

where $u_{I,1} = 0$, and $L(z)$ and $Q(z)$ are the learning and robustness filters, respectively. Here, α is the learning gain, and $u_{I,k}$ and e_k denote the ILC control input and the tracking error at the kth iteration, respectively. The tracking results of the kth iteration are available for the update law at the $(k+1)$th iteration. In this approach, $u_{I,k+1}$ is calculated using (10) and augmented to the feedback control input in the current iteration. To guarantee convergence of the ILC algorithm in the iteration domain, tracking error and control inputs must remain bounded

IEEE Proof

in the presence of uncertainties. According to Fig. 4(b), we have

$$\begin{aligned} e_{k+1} &= y_d - y_{k+1} - n_{k+1} \\ u_{k+1} &= u_{C,k+1} + u_{I,k+1} \\ y_{k+1} &= u_{k+1} G_d(z) + d_p. \end{aligned} \tag{11}$$

For simplicity, we discard (z) in the following formulations. To analyze the effect of noise on the steady-state tracking error and convergence, we assume that measurement noise is varying through iterations and uniformly bounded at each iteration, i.e., $|n_k| \leq \delta$. Accordingly, the ILC algorithm converges if the ILC filters are designed such that

$$|Q(1 - \alpha LSG_d)| < 1 \tag{12}$$

and accordingly, the asymptotic error at convergence is bounded by

$$\begin{aligned} e_\infty = \lim_{k\to\infty} |e_k| \leq \frac{|S(1-Q)|}{1-\rho}|y_d - d_p| \\ + \frac{|\alpha SQLSG_d|}{1-\rho}|\delta| + |S||\delta| \end{aligned} \tag{13}$$

where $\rho = Q(1 - \alpha LSG_d)$ and S is the sensitivity function. For the proof and details; see Appendix.

1) Design of Learning Filter L: A number of techniques have been proposed to design the learning filter [24]. According to (22), the learning filter is selected so that

$$L = (SG_d)^{-1}. \tag{14}$$

Therefore, the algorithm converges in one iteration assuming $Q = 1$ and ignoring the effect of noise. The challenge with this technique is the NMP zeros of the plant. NMP zeros are inevitable when the plant is discretized at a certain sampling frequency or when the sensors and actuators are not collocated. To determine stable approximate inversion, well-established techniques such as NMP zeros ignore (NPZ-ignore), zero magnitude error tracking controller (ZMETC), and zero-phase error tracking controller (ZPETC) have been employed [43], [44]. These techniques are straightforward and effective in achieving the desired tracking performance. The NPZ-ignore algorithm ignores a part of system dynamics and, hence, is less accurate than other methods. ZMETC and ZPETC approximate the effect of NMP zero by a stable zero and a stable pole, respectively. The type of the system, the location of NMP zeros, and the nature of the application determine the algorithm most suitable for the approximate inversion [43].

Anticausal filtering [45] or stable inversion [44], [46] are alternatives to inverse approximation methods. They can significantly improve the tracking results. These approaches are based on partitioning the model into two parts consisting of the minimum-phase and NMP zeros. Inversion of the first part is straightforward. However, stable inverse of the second part is anticausal. To perform anticausal filtering, we can replace z with z^{-1} and apply the filter on the time-reversed input sequence.

Here, we explore the performance of ZMETC and anticausal filtering approaches in designing the learning filter. To obtain L using ZMETC, we define $H(z) = S(z)G_d(z)$, i.e.

$$H(z) = \frac{B_s(z)B_u(z)}{A(z)} \tag{15}$$

where $A(z)$ incorporates poles and $B_s(z)$ and $B_u(z)$ include stable and unstable zeros, respectively. Since $H(z)$ is a proper transfer function, we omit the units of delay considered for causal implementation. Here, $B_u(z)$ is a polynomial written as $B_u(z) = b_{u_n} z^n + b_{u_{n-1}} z^{n-1} + \cdots + b_{u_0}$. According to ZMETC, the approximate inverse of $H(z)$ can be obtained by reflecting unstable zeros to stable ones with respect to the unit circle, i.e., $z_{u_i} \to 1/z_{u_i}$. Therefore, $\tilde{H}^{-1}(z)$ can be obtained as

$$\tilde{H}^{-1}(z) = \frac{A(z)}{B_s(z)B_u^\star(z)} \tag{16}$$

where $B_u^\star(z) = b_{u_0} z^n + b_{u_1} z^{n-1} + \cdots + b_{u_n}$. Note that dc gain adjustment is not required since the dc gain remains unchanged.

In anticausal filtering approach [45], $H(z)$ can be factorized into

$$H(z) = H_s(z)H_u(z) \tag{17}$$

where $H_s(z)$ and $H_u(z)$ contain the invertible and noninvertible zeros, respectively. Accordingly, $H_s^{-1}(z)$ is stable and causal, while $H_u^{-1}(z)$ is stable and anticausal. Since the ILC algorithm is applied offline, and the tracking error is available from the previous iteration, we may determine L by anticausal filtering approach. From (10) and (17), we may write

$$w_k(t) = H_s^{-1}(z)e_k(t) \tag{18}$$

then, the anticausal filtering can be implemented by reversing the sequence, $w_k(t)$, and applying the causal filter, i.e.

$$v_k(t) = H_u^{-1}(z^{-1})w_k(N - t). \tag{19}$$

Finally, the filtered output is obtained by reversing $v_k(t)$, i.e., $z_k(t) = v_k(N - t)$. Thus, the ILC control update law in (10) can be rewritten as

$$u_{I,k+1}(z) = Q(z)[u_{I,k}(z) + \alpha z_k], \quad k \geq 1. \tag{20}$$

The anticausal filtering method inverts SG_d implicitly and determines the learning filter. Therefore, the ILC algorithm converges fast and yields smaller tracking error in comparison with the ZMETC, which suffers from approximation error.

2) Design of Robustness Filter Q: According to (13), tracking error approaches zero asymptotically if $Q = 1$ and $|\delta| \approx 0$. In practice, however, $|\delta| \neq 0$ and the Q-filter is typically selected as a low-pass filter to mitigate nonrepeating disturbances and high-frequency noise. The cut-off frequency of Q, on the other hand, should be large enough to include reference frequencies and disturbances. In this case, Q can effectively minimize the deterministic component of the tracking error. It is clear from (13) that in order to minimize the effect of disturbances and noise, we must have $|S(1 - Q)| < 1$ and $|SQ| < 1$. This requires a compromise in designing Q. As discussed in [47], the variance of error at convergence is limited by the variance of iteration varying noise and disturbances. The variance can be reduced by selecting the learning gain as $0 < \alpha \leq 1$. This will ensure that the ILC algorithm will converge with a small tracking error in the

IEEE Proof

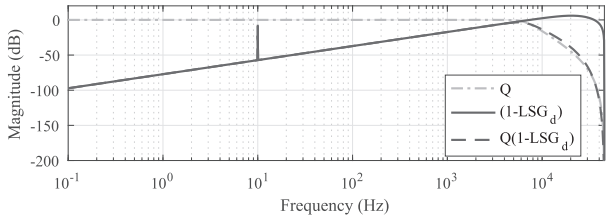

Fig. 6. Magnitude of the low-pass Q-filter, $|1 - LSG_d|$ and $|Q(1 - LSG_d)|$ when the ZMETC technique is employed to design the learning filter for tracking the rosette pattern at 10 fps.

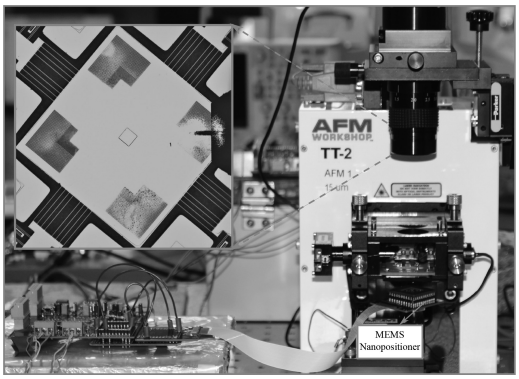

Fig. 7. Experimental setup consists of a MEMS nanopositioner integrated into a commercial AFM. The inset shows the contact-mode cantilever landed on the gold features microfabricated on the scan table [18].

presence of iteration varying noise and disturbances. Decreasing the learning gain will also reduce the convergence rate.

Here, a fourth-order Butterworth filter is used as the Q-filter. The bandwidth of the filter is selected as 5 kHz, 6.5 kHz, 8.5 kHz, and 11 kHz at 5 fps, 10 fps, 15 fps, and 20 fps, respectively. Accordingly, Q-filter ensures the stability and convergence of the ILC algorithm when the ZMETC technique is applied. As shown in Fig. 6, the Q-filter makes $|1 - \alpha LSG_d|$ small at higher frequencies. To avoid any distortion in the output signal due to the phase shift imposed by the filter, a zero-phase filtering is employed using *filtfilt*$(\cdot)$ function in MATLAB.

Since the filter bandwidth is large at high frame rates to encompass higher harmonics, the tracking error may not decrease monotonically due to the high-frequency noise. To address this issue, α is set to 0.7 and 0.5 at 15 fps and 20 fps, respectively, and to unity at 5 fps and 10 fps.

IV. Experiment

To evaluate the performance of the proposed control scheme, we conducted tracking experiments at 5 fps, 10 fps, 15 fps, and 20 fps using a feedback-controlled MEMS nanopositioner, as shown in Fig. 7. In this section, we present the experimental results and discuss the performance of two inversion techniques in tracking the rosette pattern.

A. Implementation

The closed-loop system is implemented in a dSPACE MicroLabBox with a sampling frequency of 90720 Hz. The control signal is amplified to drive the lateral axes of the nanopositioner

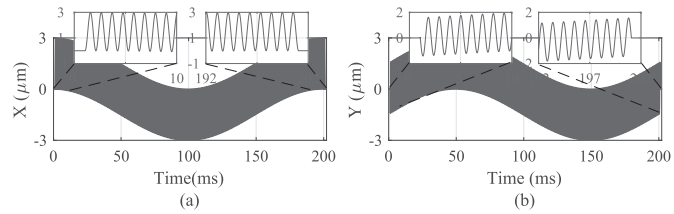

Fig. 8. Reference signals of rosette pattern at 5 fps after zero padding.

and the stage displacement is measured using the sensor output's voltage and predetermined calibration factors. To implement the ILC, we require an interface to communicate between the hardware and the software. ASAM XIL API is a standard utilized in dSPACE to facilitate such communications. Specifically, we used the XIL API model access port to gain access to the SIMULINK model, write into the blocks, and capture signals. We then used the XIL API. NET implementation as a high-level program in a MATLAB script to implement the ILC algorithm, and to read and manipulate the variables online. Initially, the ILC control input is set to zero and the IMBC is employed in the tracking experiment. Then, the experiment is continued iteratively and the desired signals including the tracking error are captured in each iteration to update the ILC control drive signal. The experiment is performed for a specific number of iterations to ensure the convergence of the ILC algorithm. We allow for 15 iterations, although the algorithm converges very fast in practice.

B. Tracking the Rosette Pattern

Since the damped plant is NMP, anticausal learning and filtering may result in transients. To address this issue, we may extend the reference signals by leading and trailing zeros, which we will truncate at the end. The number of zeros N_z is determined such that the imaging rate for single-frame scanning remains almost unchanged. Note that no zero is added to intermediate frames in sequential scanning. Consequently, the extended reference signals, in a single-frame scan, are obtained as

$$x_a(t),\, y_a(t) = \begin{cases} 0 & 0 \le t \le \Delta \\ x(t),\, y(t) & \Delta \le t \le T + \Delta \\ 0 & T + \Delta \le t \le T + 2\Delta \end{cases} \tag{21}$$

where $\Delta = N_z f_s$ and f_s is the sampling frequency. Based on the expected transient time, we select $\Delta = 1/f_1$ with f_1 as described by (2). This extends the scan time to $T + 2\Delta$. Fig. 8 shows the reference signals at 5 fps after zero-padding. In a single-frame scanning, the scan time increases by 1 %, which is negligible.

C. Experimental Results

Initially, we perform closed-loop experiments to track a single frame of the rosette pattern generated by the reference signals in (21). Fig. 9 shows the root-mean-square (RMS) value of tracking error at each iteration and the close-up views indicate the tracking error at convergence. Note that the RMS value of error at the first iteration is corresponding to the IMBC when the ILC is inactive. We observe that the learning algorithm converges quickly,

IEEE Proof

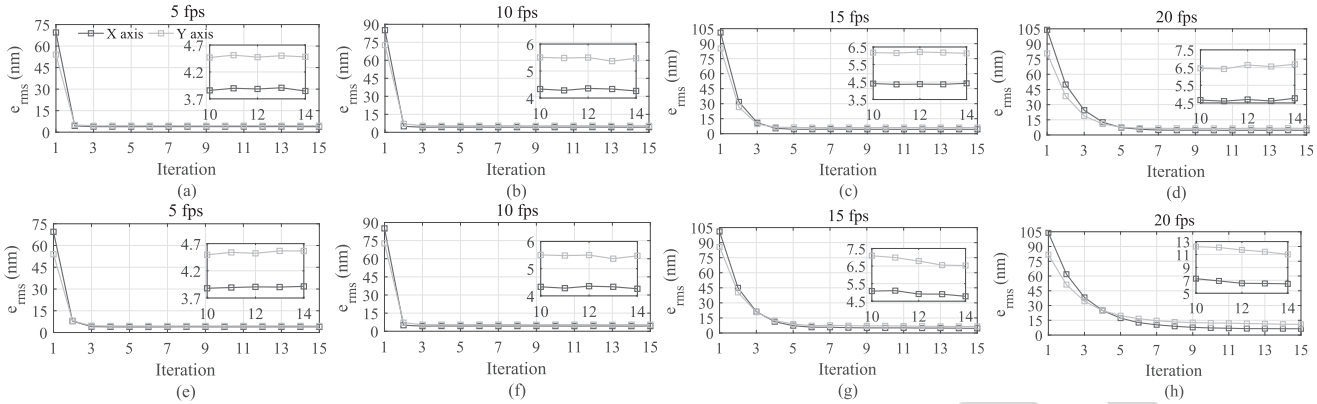

Fig. 9. RMS value of error at each iteration when the anticausal filtering approach (a) to (d) and ZMETC technique (e) to (h) have been employed to determine the learning filter L at (a) and (e) 5 fps, (b) and (f) 10 fps, (c) and (g) 15 fps, (d) and (h) 20 fps.

TABLE II
RMS VALUE OF TRACKING ERROR INCLUDING THE TRANSIENTS AT ALL FRAME RATES

Frame rate (fps)	IMBC		IMBC+ILC			
			Anti-causal		ZMETC	
	e_x(nm)	e_y(nm)	e_x(nm)	e_y(nm)	e_x(nm)	e_y(nm)
5	69.5	54.1	3.9	4.5	3.9	4.5
10	85.1	75.7	4.3	5.4	4.6	5.7
15	101.0	85.2	4.4	6.2	5.0	6.8
20	104.0	80.7	4.7	6.5	6.4	11.9

and tracking error decreases monotonically through iterations with both inversion techniques. At low frame rates, the algorithm converges in less than three iterations, while it takes five to seven iterations for the tracking error to approach the asymptotic value at higher frame rates. It is clear that the learning rate is faster at 5 fps and 10 fps since $\alpha = 1$. Fig. 9(a)–(d) describes a fast convergence rate with the anticausal filtering approach, whereas it takes slightly longer for the algorithm to converge using the ZMETC technique, particularly at higher frame rates; see Fig. 9(e)–(h). It appears that the accuracy of ZMETC degrades at 20 fps as the higher harmonics of the reference frequency lie beyond the bandwidth of the plant resulting in an approximation error. Since single-fame scanning is also performed here, we consider both the transient and steady-state errors in calculation of the RMS values. From experimental results, we observe that the combination of ILC with IMBC properly minimizes the transient and steady-state error at convergence.

Table II presents the RMS value of tracking error with the proposed control scheme. We achieve 90 % improvement with ILC using the anticausal filtering approach. Moreover, the RMS value of tracking error decreases to less than 0.1 % of the scan diameter. Considering the fact that IMBC restricts the sensor noise and bounds the tracking error at the first iteration, integrating the ILC with the IMBC enhances the tracking performance.

To evaluate the efficacy of the proposed control scheme in rejecting the repetitive disturbances, we obtain FFT of the tracking error. Fig. 10 shows FFT of tracking error with anticausal filtering and ZMETC approaches at all frame rates. The closeup views reveal that the ILC precisely removes the higher harmonics not compensated by the IMBC alone. Both inversion techniques yield a good tracking performance, however, assuming identical gains, the anticausal filtering approach outperforms ZMETC at high frame rates; see Fig. 10(h). We observe that at 20 fps fundamental harmonic at f_1 has been removed satisfactorily, however, the second harmonic at 7560 Hz is still dominant in the error.

Fig. 11 depicts the time-domain results for single-frame tracking of the rosette pattern. Because of its effectiveness, here we report the time-domain results with the anticausal filtering only. Note that the padded zeros are truncated from the results. The integration of ILC with IMBC leads to a visible improvement in tracking. We also observe that IMBC leaves a steady-state error in the y-axis when the ILC is off. Although the nanopositioner dynamics are very similar in x and y axes, the y-axis closed-loop system with IMBC cannot follow the low-frequency reference signal in one scan period. Augmenting the tracking controller with integral action may address the issue, but the ILC eliminates the y-axis steady-state error successfully.

As illustrated in the close-up views of Fig. 11, a large peak appears at the beginning and end of y-axis tracking error during single-frame scans. This is due to the nonzero steady-state tracking error and the backward–forward technique used to implement the learning and robustness filters. To prevent the peak of error from affecting single-frame scans, we provide *a priori* learning using the pattern's periodicity. We extend the length of the reference signals by replacing T with $T + 2\epsilon$ in (21). Here, ϵ is selected as $1/f_1$ to cover the transient duration. In this case, the scan time for single-frame scanning increases by less than 2 %. In sequential scanning, consecutive frames are not affected by the error peak meaning that the scan time of successive frames remains unchanged. Therefore, the overall scan time will be $T_f = N_f T + 2\Delta + 2\epsilon$, where N_f is the total number of frames.

Steady-state tracking errors in Table III allows us to compare the performance of proposed control structure with the IMBC during sequential rosette scan assuming that the transient response is disappeared. Combined ILC/IMBC reduces the peak to peak value of steady-state error by 50 % and keeping it below

IEEE Proof

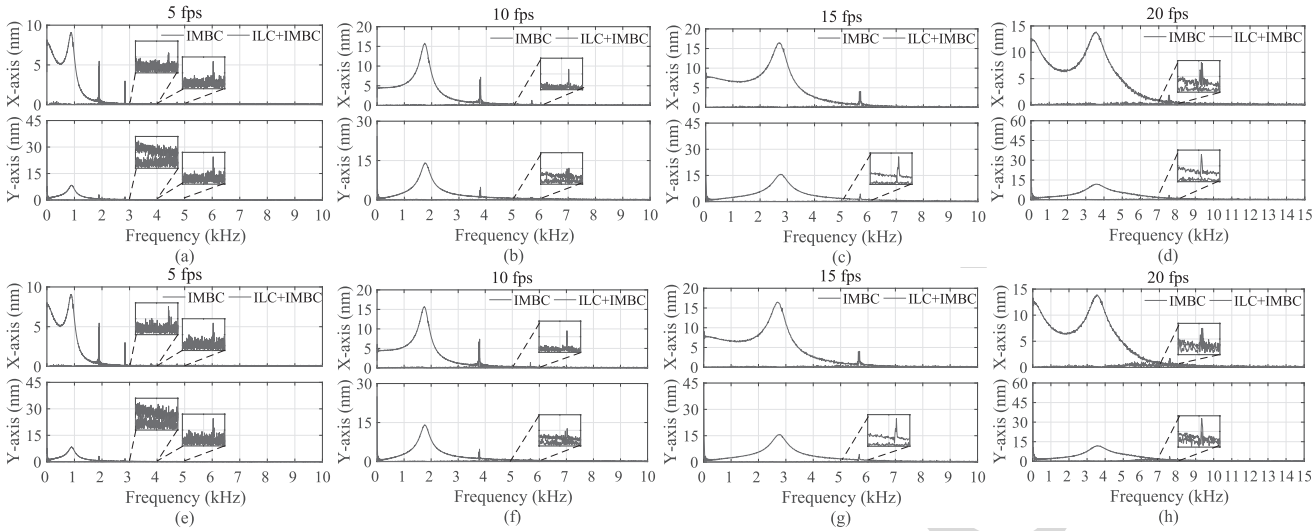

Fig. 10. FFT of tracking error with IMBC and the combination of ILC and IMBC when the anticausal filtering approach (a) to (d) and ZMETC technique (e) to (h) are employed to determine the learning filter (L) at 5 fps, 10 fps, 15 fps, and 20 fps.

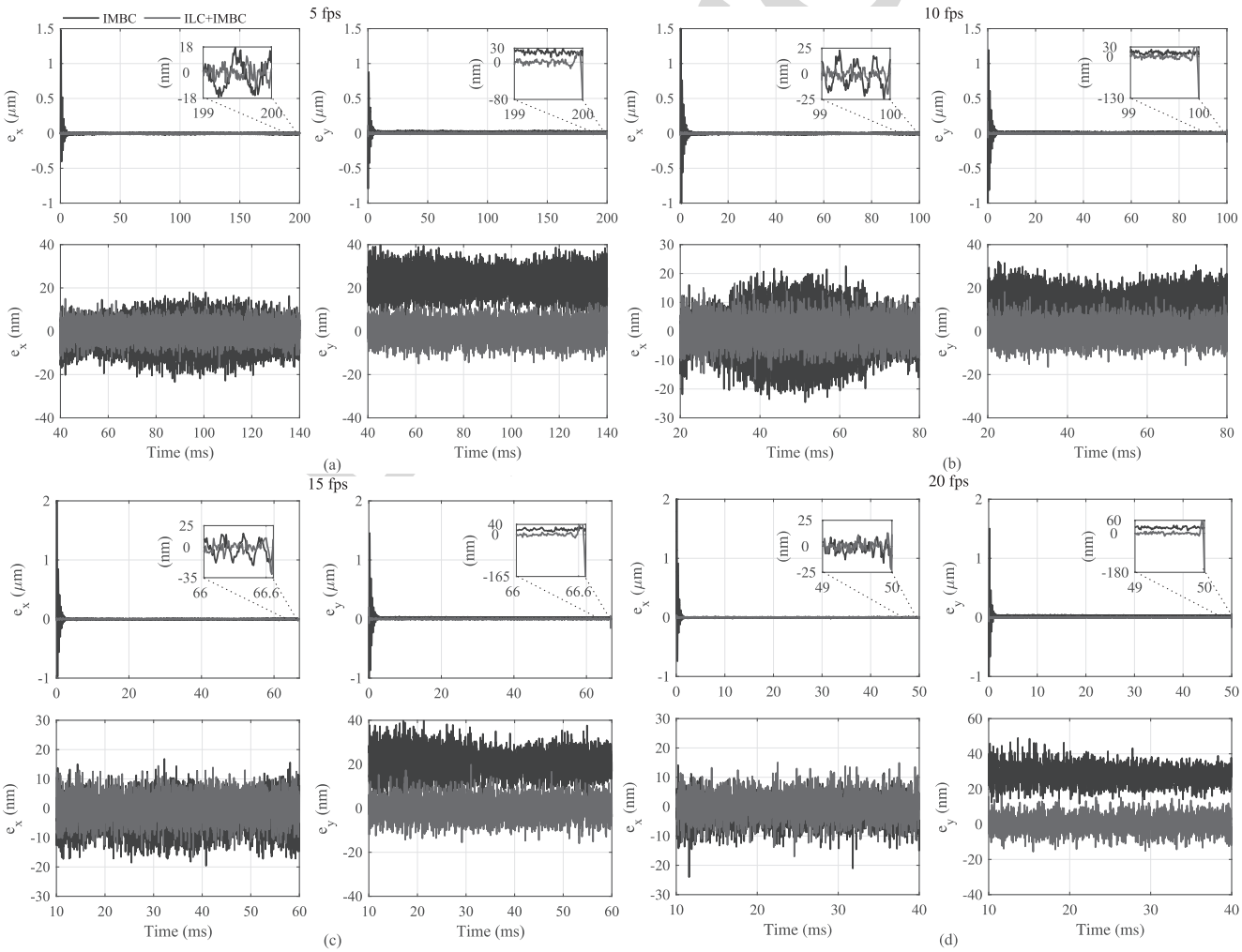

Fig. 11. Time-domain tracking results of single-frame scan at (a) 5 fps, (b) 10 fps, (c) 15 fps, and (d) 20 fps when the anticausal filtering approach is employed to determine the learning filter.

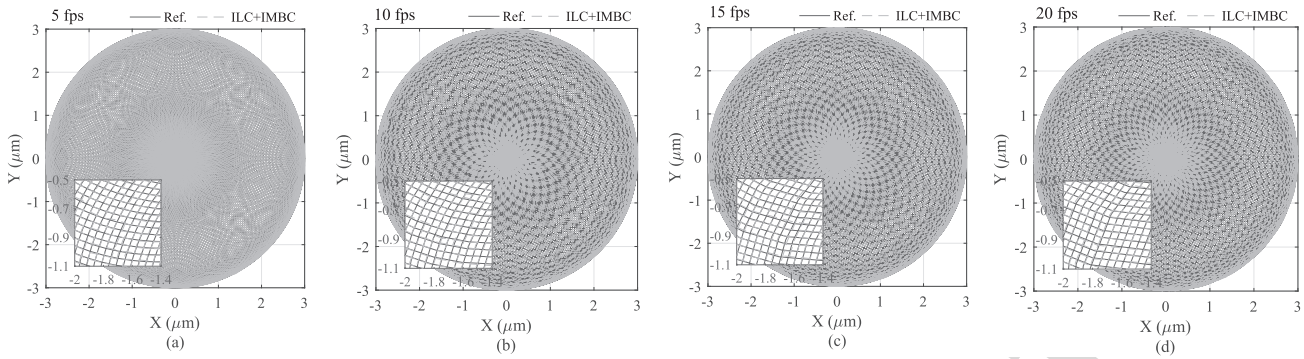

Fig. 12. Reference and actual rosette trajectory at (a) 5 fps, (b) 10 fps, (c) 15 fps, and (d) 20 fps.

TABLE III
RMS VALUE OF STEADY-STATE TRACKING ERROR AT ALL FRAME RATES

Frame rate (fps)	IMBC		IMBC+ILC			
			Anti-causal		ZMETC	
	e_x(nm)	e_y(nm)	e_x(nm)	e_y(nm)	e_x(nm)	e_y(nm)
5	8.2	23.3	3.8	4.2	3.8	4.2
10	9.4	13.8	4.2	4.5	4.5	4.7
15	7.2	21.3	4.3	4.6	4.6	4.8
20	5.7	30.2	4.2	4.8	5.5	7.1

20 nm. In addition, this method improves the x- and y-axis tracking errors by more than 27 % and 79 %, respectively.

As discussed in Section III-C, RMS value of tracking error at convergence is bounded by iteration varying noise and disturbances. According to (13), $e_\infty \leq 2|S||\delta|$ if $Q = 1$, and $L = (SG_d)^{-1}$. Therefore, asymptotic error relies on the sensor output noise fed back to the system. Since IMBC attenuates the high-frequency projected noise, the upper bound on the ultimate error determines the resolution of the displacement sensors. To obtain sensor resolution in open loop and under damping, we recorded sensor output noise for 60 s at a sampling frequency of 62.5 kHz with an antialiasing filter (Stanford Research SR650 low-noise filter) with a cut-off frequency of 15 kHz being used in the path. To reject noise and electrical disturbances, the experiment was performed in a closed metal box. Open-loop RMS value of noise is 2 nm, with the actuators electrically grounded, and it is about 3 nm with the damping loop being active. Asymptotic error obtained with the anticausal filtering approach is bounded by about 4 nm, which is close to the sensor noise floor.

The rosette trajectory and the actual displacement of the stage tracing the rosette pattern are depicted in Fig. 12. Close-up views validate the tracking performance at all frame rates when the ILC is integrated with the internal-model-based controller.

V. AFM IMAGING

To implement rosette scanning with the proposed control scheme, we used an AFMWorkshop TT-AFM. We mounted an MEMS nanopositioner on the AFM 3-DOF positioning mechanism. The MEMS device serves as the scanner in the experiments reported here. As indicated in the inset of Fig. 7, the periodic gold features fabricated on the scan table of the MEMS nanopositioner were used as the sample. Dimensions of the gratings is $4 \times 4 \times 0.5\,\mu\text{m}^3$ with a pitch of $3\,\mu$m [5]. Due to the low z-axis bandwidth of the commercial AFM's positioner, we performed the experiments in constant-height contact mode. We used a contact-mode cantilever with a resonance frequency of about 27.8 kHz and stiffness of 0.25 N/m. When the cantilever was landed on the MEMS scan table, we closed the control loop and activated the iterative learning algorithm. X and Y sensor outputs and cantilever deflection were recorded simultaneously to construct 3-D AFM images. Fig. 13 depicts a single-frame of rosette scan at frame rates ranging from 5 to 20 fps, indicating that AFM images have precisely captured the structure of a gold feature.

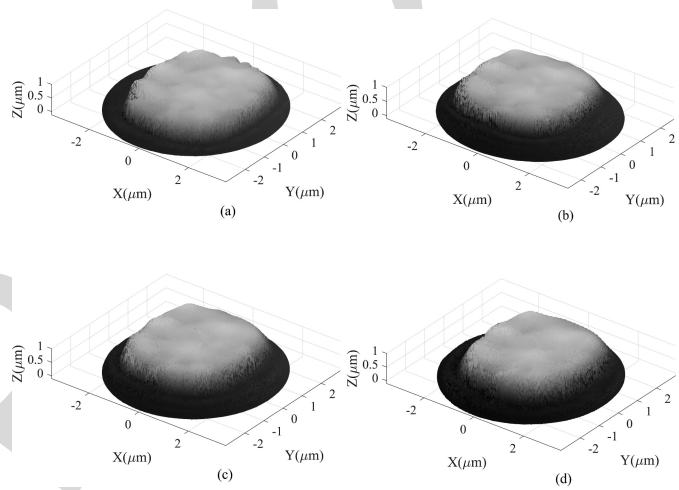

Fig. 13. 3-D AFM images acquired with rosette-scan at (a) 5 fps, (b) 10 fps, (c) 15 fps, and (d) 20 fps on a window size of 6 μm.

We also performed sequential scanning at video rate. To imitate a dynamic process, the AFM positioner was made to raster at 0.2 Hz over a window size of $6 \times 6\,\mu\text{m}^2$ while the MEMS nanopositioner was following the rosette pattern at 20 fps in a scan area with a diameter of 6 μm. Fig. 14 illustrates a series of AFM time-lapsed images that capture the gold feature moving slowly under the cantilever.

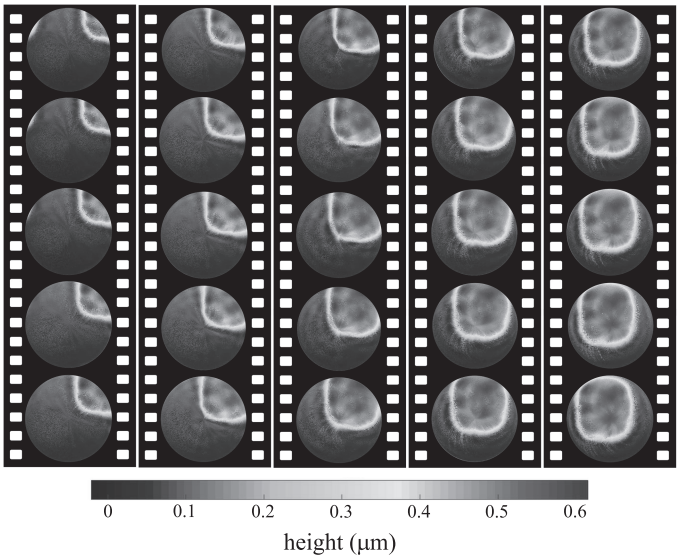

Fig. 14. Series of rosette-scan frames at 20 fps captured in constant-height contact mode on a window size with a diameter of 6 μm.

VI. Conclusion

We demonstrate video-rate rosette scanning by combining an internal-model-based controller with an iterative learning controller. The feedback controller contains an internal model of the reference signals and limits the closed-loop bandwidth to bound the tracking error when the ILC is OFF. The ILC is used to mitigate induced disturbances originating from inherent system nonlinearities. The model-based ILC is designed using well-established inversion techniques. The experimental results validate the efficacy of the control scheme in reducing transient and steady-state tracking errors at several frame rates. We show that this control scheme is suitable for both sequential and single-frame scanning. We acquire successive AFM images of slowly moving gold features at 20 fps in constant-height contact mode. In future works, we will implement the scanning experiment in constant-force contact mode and tapping mode using a high-bandwidth z-axis positioner.

Appendix

According to (11), the tracking error in the $(k+1)$th iteration can be described as

$$e_{k+1} = Q(1-\alpha LSG_d)e_k + S(1-Q)(y_d - d_p) + SQn_k - Sn_{k+1}. \tag{22}$$

Proceeding through iterations, we can derive the relationship between e_{k+1} and e_1 as

$$e_{k+1} = \rho^k e_1 + \sum_{i=0}^{k-1} S(1-Q)(y_d - d_p)\rho^i + \sum_{i=0}^{k-1} SQ\rho^i n_{k-i} - \sum_{i=0}^{k-1} S\rho^i n_{k+1-i} \tag{23}$$

where $\rho = Q(1-\alpha LSG_d)$. By changing the index variable, the last two terms can be combined into one, hence, (23) can be simplified to

$$e_{k+1} = \rho^k e_1 + S(1-Q)(y_d - d_p)\sum_{i=0}^{k-1}\rho^i + SQLSG_d\sum_{i=0}^{k-1}\rho^i n_{k-i} - Sn_{k+1} + \rho^k n_1. \tag{24}$$

Assuming $|n_k| \le \delta$, the upper bound on e_{k+1} is obtained as

$$|e_{k+1}| \le |\rho|^k|e_1| + |S(1-Q)||y_d - d_p|\sum_{i=0}^{k-1}|\rho|^i + |SQLSG_d|\sum_{i=0}^{k-1}|\rho|^i|\delta| - |S||\delta| + |\rho|^k|\delta|. \tag{25}$$

Since the feedback controller is designed to keep the tracking error small at the first iteration, $|e_1|$ is bounded. As a result, (25) implies that the asymptotic error is bounded when $k \to \infty$ if $|\rho| < 1$.

Acknowledgment

Disclaimer: This article was prepared as an account of work sponsored by an agency of the United States Government. Neither the U.S. Government nor any agency thereof, nor any of their employees, makes any warranty, express or implied, or assumes any legal liability or responsibility for the accuracy, completeness, or usefulness of any information, apparatus, product, or process disclosed, or represents that its use would not infringe privately owned rights. Reference herein to any specific commercial product, process, or service by trade name, trademark, manufacturer, or otherwise does not necessarily constitute or imply its endorsement, recommendation, or favoring by the U.S. Government or any agency thereof. The views and opinions of authors expressed herein do not necessarily state or reflect those of the U.S. Government or any agency thereof.

References

[1] N. Kodera and T. Ando, "The path to visualization of walking myosin v by high-speed atomic force microscopy," *Biophys. Rev.*, vol. 6, no. 3, pp. 237–260, 2014.

[2] K. Ariga, T. Mori, and L. K. Shrestha, "Nanoarchitectonics from molecular units to living-creature-like motifs," *Chem. Rec.*, vol. 18, no. 7/8, pp. 676–695, 2018.

[3] Y. Du, J. Pan, and J. H. Choi, "A review on optical imaging of DNA nanostructures and dynamic processes," *Methods Appl. Fluorescence*, vol. 7, no. 1, 2019, Art. no. 012002.

[4] T. Ando, "Directly watching biomolecules in action by high-speed atomic force microscopy," *Biophys. Rev.*, vol. 9, no. 4, pp. 421–429, 2017.

[5] M. Maroufi and S. O. R. Moheimani, "A 2DOF SOI-MEMS nanopositioner with tilted flexure bulk piezoresistive displacement sensors," *IEEE Sensors J.*, vol. 16, no. 7, pp. 1908–1917, Apr. 2016.

[6] S. Watanabe and T. Ando, "High-speed xyz-nanopositioner for scanning ion conductance microscopy," *Appl. Phys. Lett.*, vol. 111, no. 11, 2017, Art. no. 113106.

[7] M. Mahdavi, N. Nikooienejad, and S. O. R. Moheimani, "AFM microcantilever with a collocated AlN sensor-actuator pair: Enabling efficient Q-control for dynamic imaging," *J. Microelectromech. Syst.*, vol. 29, no. 5, pp. 661–668, 2020.

IEEE Proof

[8] A. Bazaei, Y. K. Yong, and S. O. R. Moheimani, "Combining spiral scanning and internal model control for sequential AFM imaging at video rate," *IEEE/ASME Trans. Mechatron.*, vol. 22, no. 1, pp. 371–380, Feb. 2017.

[9] Y. Wu, Y. Fang, X. Ren, and H. Lu, "A wavelet-based AFM fast imaging method with self-tuning scanning frequency," *IEEE Trans. Nanotechnol.*, vol. 16, no. 6, pp. 1088–1098, Nov. 2017.

[10] A. Bazaei, Y. K. Yong, and S. O. R. Moheimani, "High-speed Lissajous-scan atomic force microscopy: Scan pattern planning and control design issues," *Rev. Sci. Instrum.*, vol. 83, no. 6, 2012, Art. no. 063701.

[11] T. Tuma, J. Lygeros, V. Kartik, A. Sebastian, and A. Pantazi, "High-Speed multiresolution scanning probe microscopy based on Lissajous scan trajectories," *Nanotechnology*, vol. 23, no. 18, 2012, Art. no. 185501.

[12] I. A. Mahmood, S. O. R. Moheimani, and B. Bhikkaji, "A new scanning method for fast atomic force microscopy," *IEEE Trans. Nanotechnol.*, vol. 10, no. 2, pp. 203–216, Mar. 2011.

[13] A. Bazaei, M. Maroufi, A. G. Fowler, and S. O. R. Moheimani, "Internal model control for spiral trajectory tracking with MEMS AFM scanners," *IEEE Trans. Control Syst. Technol.*, vol. 24, no. 5, pp. 1717–1728, Sep. 2016.

[14] D. Ziegler, T. R. Meyer, A. Amrein, A. L. Bertozzi, and P. D. Ashby, "Ideal scan path for high-speed atomic force microscopy," *IEEE/ASME Trans. Mechatron.*, vol. 22, no. 1, pp. 381–391, Feb. 2017.

[15] Y. K. Yong, S. O. R. Moheimani, and I. R. Petersen, "High-speed cycloid-scan atomic force microscopy," *Nanotechnology*, vol. 21, no. 36, 2010, Art. no. 365503.

[16] N. Nikooienejad, A. Alipour, M. Maroufi, and S. O. R. Moheimani, "Video-rate non-raster AFM imaging with cycloid trajectory," *IEEE Trans. Control Syst. Technol.*, vol. 28, no. 2, pp. 436–447, Mar. 2020.

[17] M. Shibata, H. Watanabe, T. Uchihashi, T. Ando, and R. Yasuda, "High-speed atomic force microscopy imaging of live mammalian cells," *Biophys. Physicobiol.*, vol. 14, pp. 127–135, 2017.

[18] N. Nikooienejad, M. Maroufi, and S. O. R. Moheimani, "Rosette-scan video-rate atomic force microscopy: Trajectory patterning and control design," *Rev. Sci. Instrum.*, vol. 90, no. 7, 2019, Art. no. 073702.

[19] M. S. Rana, H. R. Pota, and I. R. Petersen, "Spiral scanning with improved control for faster imaging of AFM," *IEEE Trans. Nanotechnol.*, vol. 13, no. 3, pp. 541–550, May 2014.

[20] A. Bazaei, M. Maroufi, and S. R. Moheimani, "Tracking control of constant-linear-velocity spiral reference by LQG method," *IFAC-PapersOnLine*, vol. 50, no. 1, pp. 15568–15573, 2017.

[21] M. G. Ruppert, M. Maroufi, A. Bazaei, and S. R. Moheimani, "Kalman filter enabled high-speed control of a MEMS nanopositioner," *IFAC-PapersOnLine*, vol. 50, no. 1, pp. 15554–15560, 2017.

[22] M. Maroufi, A. G. Fowler, A. Bazaei, and S. O. R. Moheimani, "High-stroke silicon-on-insulator MEMS nanopositioner: Control design for non-raster scan atomic force microscopy," *Rev. Sci. Instrum.*, vol. 86, no. 2, 2015, Art. no. 023705.

[23] S. Arimoto, S. Kawamura, and F. Miyazaki, "Bettering operation of robots by learning," *J. Robot. Syst.*, vol. 1, no. 2, pp. 123–140, 1984.

[24] D. A. Bristow, M. Tharayil, and A. G. Alleyne, "A survey of iterative learning control," *IEEE Control Syst. Mag.*, vol. 26, no. 3, pp. 96–114, Jun. 2006.

[25] F. Boeren, A. Bareja, T. Kok, and T. Oomen, "Frequency-domain ILC approach for repeating and varying tasks: With application to semiconductor bonding equipment," *IEEE/ASME Trans. Mechatron.*, vol. 21, no. 6, pp. 2716–2727, Dec. 2016.

[26] Z. Wang, C. P. Pannier, K. Barton, and D. J. Hoelzle, "Application of robust monotonically convergent spatial iterative learning control to microscale additive manufacturing," *Mechatronics*, vol. 56, pp. 157–165, 2018.

[27] Q. Zhu, F. Song, J. Xu, and Y. Liu, "An internal model based iterative learning control for wafer scanner systems," *IEEE/ASME Trans. Mechatron.*, vol. 24, no. 5, pp. 2073–2084, Oct. 2019.

[28] J. van Zundert, J. Bolder, and T. Oomen, "Optimality and flexibility in iterative learning control for varying tasks," *Automatica*, vol. 67, pp. 295–302, 2016.

[29] V. Dao and S. Chen, "Helical contouring control with online iterative learning control," in *Proc. IEEE/ASME Int. Conf. Adv. Intell. Mechatron.*, 2018, pp. 599–603.

[30] Y. Chen, K. L. Moore, J. Yu, and T. Zhang, "Iterative learning control and repetitive control in hard disk drive industry—A tutorial," in *Proc. IEEE Conf. Decis. Control*, 2006, pp. 2338–2351.

[31] K. K. Leang and S. Devasia, "Design of hysteresis-compensating iterative learning control for piezo-positioners: Application to atomic force microscopes," *Mechatronics*, vol. 16, no. 3, pp. 141–158, 2006.

[32] Y. Wu and Q. Zou, "Iterative control approach to compensate for both the hysteresis and the dynamics effects of piezo actuators," *IEEE Trans. Control Syst. Technol.*, vol. 15, no. 5, pp. 936–944, Sep. 2007.

[33] Y. Wu, Q. Zou, and C. Su, "A current cycle feedback iterative learning control approach for AFM imaging," *IEEE Trans. Nanotechnol.*, vol. 8, no. 4, pp. 515–527, Jul. 2009.

[34] D. Huang, J. Xu, V. Venkataramanan, and T. C. T. Huynh, "High-performance tracking of piezoelectric positioning stage using current-cycle iterative learning control with gain scheduling," *IEEE Trans. Ind. Electron.*, vol. 61, no. 2, pp. 1085–1098, Feb. 2014.

[35] Y. Jian, D. Huang, J. Liu, and D. Min, "High-precision tracking of piezoelectric actuator using iterative learning control and direct inverse compensation of hysteresis," *IEEE Trans. Ind. Electron.*, vol. 66, no. 1, pp. 368–377, Jan. 2019.

[36] S. Xie and J. Ren, "High-speed AFM imaging via iterative learning-based model predictive control," *Mechatronics*, vol. 57, pp. 86–94, 2019.

[37] M. S. de Oliveira and A. T. Salton, "Iterative learning control for spiral scanning patterns in atomic force microscopy," in *Intelligent Robotics and Applications*. Berlin, Germany: Springer, 2018, pp. 389–399.

[38] J. Ling, Z. Feng, M. Ming, Z. Guo, and X. Xiao, "Integrating damping control with iterative learning control for fast and precise scanning of nanopositioners: A TITO design*," in *Proc. Int. Conf. Adv. Robot. Mechatron.*, 2018, pp. 183–188.

[39] H. Xie, Y. Wen, X. Shen, H. Zhang, and L. Sun, "High-speed AFM imaging of nanopositioning stages using H_∞ and iterative learning control," *IEEE Trans. Ind. Electron.*, vol. 67, no. 3, pp. 2430–2439, Mar. 2020.

[40] N. Nikooienejad, M. Maroufi, and S. O. R. Moheimani, "Iterative learning control for high-speed rosette trajectory tracking," in *Proc. IEEE Conf. Decis. Control*, 2019, pp. 6832–6837.

[41] M. Maroufi, A. Bazaei, A. Mohammadi, and S. O. R. Moheimani, "Tilted beam piezoresistive displacement sensor: Design, modeling, and characterization," *J. Microelectromech. Syst.*, vol. 24, no. 5, pp. 1594–1605, 2015.

[42] B. Francis and W. Wonham, "The internal model principle of control theory," *Automatica*, vol. 12, no. 5, pp. 457–465, 1976.

[43] J. Butterworth, L. Pao, and D. Abramovitch, "Analysis and comparison of three discrete-time feedforward model-inverse control techniques for nonminimum-phase systems," *Mechatronics*, vol. 22, no. 5, pp. 577–587, 2012.

[44] J. van Zundert and T. Oomen, "On inversion-based approaches for feed-forward and ILC," *Mechatronics*, vol. 50, pp. 282–291, 2018.

[45] O. Markusson, H. Hjalmarsson, and M. Norrlof, "Iterative learning control of nonlinear non-minimum phase systems and its application to system and model inversion," in *Proc. IEEE Conf. Decis. Control*, 2001, vol. 5, pp. 4481–4482.

[46] R. de Rozario, A. J. Fleming, and T. Oomen, "Finite-time learning control using frequency response data with application to a nanopositioning stage," *IEEE/ASME Trans. Mechatron.*, vol. 24, no. 5, pp. 2085–2096, Oct. 2019.

[47] M. Butcher, A. Karimi, and R. Longchamp, "A statistical analysis of certain iterative learning control algorithms," *Int. J. Control*, vol. 81, no. 1, pp. 156–166, 2008.

Nastaran Nikooienejad received the B.Sc. and M.Sc. degrees in electrical engineering from Shiraz University and Amirkabir University of Technology, in 2006 and 2009, respectively. She is currently working toward the Ph.D. degree in electrical engineering from the University of Texas at Dallas.

Her research interests include high-precision control of MEMS devices, video-rate atomic force microscopy, and signal and image processing.

IEEE Proof

Mohammad Maroufi received the double B.Sc. degrees in mechanical engineering and applied physics and the master's degree in mechatronics from the Amirkabir University of Technology (Tehran Polytechnic), Tehran, Iran, in 2008 and 2011, respectively, and the Ph.D. degree in electrical engineering from the University of Newcastle, Callaghan, NSW, Australia, in 2015.

From 2015 to 2019, he continued his career as the Research Associate and then Research Scientist Postdoctoral appointments with the University of Texas at Dallas, Richardson, TX, USA. He is currently a Motion Sensing Hardware Engineer with the Consumer Electronics Industry. His research interests include development of ultrahigh-precision mechatronic systems and design and control of MEMS nanopositioners.

S. O. Reza Moheimani (Fellow, IEEE) received the Ph.D. in electrical engineering from the University of New South Wales, Australia, in 1996.

He currently holds the James Von Ehr Distinguished Chair in Science and Technology with the Department of Systems Engineering, University of Texas at Dallas with appointments in Electrical and Computer Engineering and Mechanical Engineering Departments. His current research interests include applications of control and estimation in high-precision mechatronic systems, high-speed scanning probe microscopy and atomically precise manufacturing of solid-state quantum devices.

Dr. Moheimani is a Fellow of IEEE, IFAC and the Institute of Physics, U.K. He is a recipient of several awards, including IFAC Nathaniel B. Nichols Medal and IEEE Control Systems Technology Award. He is the Editor-in-Chief of Mechatronics.

IEEE Proof